universität wien

MASTERARBEIT / MASTER'S THESIS

Titel der Masterarbeit / Title of the Master's Thesis

Reconstruction of Callisto's Valhalla basin using n-body and SPH simulations

verfasst von / submitted by

Philip Matthias Winter, BSc

angestrebter akademischer Grad / in partial fulfilment of the requirements for the degree of

Master of Science (MSc)

Wien, 2017 / Vienna 2017

Studienkennzahl lt. Studienblatt / degree programme code as it appears on the student record sheet:	A 066 861
Studienrichtung lt. Studienblatt / degree programme as it appears on the student record sheet:	Masterstudium Astronomie
Betreut von / Supervisor:	ao. Univ.-Prof. i.R. tit. Univ.-Prof. Dr. Rudolf Dvorak
Mitbetreut von / Co-Supervisor:	Mag. Dr. Thomas Maindl

We present results of n-body and Smooth Particle Hydrodynamics (SPH) simulations, exploring the crater formation process of the Valhalla crater located on the Jovian moon Callisto. We find typical impact velocities and impact angles which we then use for the SPH simulations to reconstruct the actual crater formation. Using a three-layered Callisto model, we find significant connections between the crater formation process and the interaction with a subsurface ocean. We also investigate into the properties of the projectile and numerical effects of low-resolution projectiles in the context of SPH.

Wir präsentieren Resultate von N-Körper und Smooth Particle Hydrodynamics (SPH) Simulationen, welche den Entstehungsprozess des Valhalla Kraters auf dem Jupitermond Kallisto behandeln. Wir finden typische Impaktgeschwindigkeiten und Impaktwinkel, welche wir für die SPH Simulationen verwenden, um die tatsächliche Kraterbildung zu rekonstruieren. Unter Verwendung eines Drei-Schichten-Modells für Kallisto finden wir signifikante Verbindungen zwischen dem Entstehungsprozess des Kraters und der Wechselwirkung mit einem unterirdischen Ozean. Wir untersuchen ebenfalls die Eigenschaften des Projektils und numerische Effekte von Projektilen bei niedriger Auflösung im Kontext von SPH.

Contents

1 Callisto - an introduction

This section gives an overview of the Galilean moon Callisto, where we focus on the history of her exploration, as well as impact craters on her surface.

1.1 Historical view

1.1.1 A brief history of Callisto

The four big moons of Jupiter were discovered by Galileo Galilei (1564-1642), an italian Astronomer. Since the moons can not be seen with the naked eye, a telescope was needed for the observation. Galileo was the first one to build such a *telescopio* which set the foundation for the modern astronomy using advanced and sensitive telescopes to explore what lays beyond Earth. After the first prototype in 1609, he developed an improved version of his telescope with which he was able to detect the four big moons of Jupiter between January 7th and 13th, 1610. As of 2017, his telescope is displayed at the *Museo Galileo* in Florence.

Galileo named the moons after the Medici family, with which he was in close contact. The current, Greek names *Io*, *Europa*, *Ganymede* and *Callisto* – who where all lovers of Zeus (Jupiter) – were first introduced by the German astronomer Simon Marius (1573-1624) a few years later. Marius discovered the moons independently from Galilei, but did not publish his results at first. Today, the moons are named by both Galilei – *Galilean moons* – and the proposal by Marius.

The discovery of the Galilean moons was the prove that not every celestial body in the Universe was moving around the Earth. Thus, the geocentric system was severely put into question. Moreover, the evidence was provided that there are other moons next to the Earth's moon in the Solar System.

The Greek word *Callisto* can be translated to *the most beautiful*. Callisto was a nymph in the Greek (Roman) Mythology and an attendant of Artemis (Diana), the godess of hunt and nature. Callisto was seduced by Zeus (Jupiter), who could not resist her beauty and disguised himself as Artemis to approach her. Due to strict chastity orders, Artemis turned her back on Callisto after it was discovered that she was pregnant (see Figure 1). After Callisto gave birth to Arcas, she was transformed into a bear by the raging and

Figure 1: *Diana bathing with her nymphs with the stories of Actaeon and Callisto* (Rembrandt van Rijn, around 1635). Callisto (on the right) defends herself as the other nymphs try to pull off her clothes and discover her pregnancy. The painting is based on stories of *The Metamorphoses* by the Roman poet Ovid.

jealous Hera (Juno). Some years later, Callisto met Arcas and tried to embrace him. But Arcas had become a hunter and just saw a wild bear approaching. He defended himself and attacked Callisto. As he had almost killed her, Zeus intervened and moved both Callisto and Arcas to the heavens, where they became the constellations Ursa Major and – depending on different interpretations – either Ursa Minor or Bootes.

1.1.2 Modern exploration

Pioneer 10 which was launched in March 1972, was the first spacecraft ever to explore the outer Solar System. It had its closest approach to Jupiter on 4 December 1973 at a speed of about $132,000\,\mathrm{km/h}$ and a distance of about $130,000\,\mathrm{km}$. It delivered the high-

est resolution images of Jupiter and its moons at the time. Approximately one year later, on 3 December 1974, Pioneer 11 had its closest approach to Jupiter, three times closer than Pioneer 10 (42, 760 km) and with a peak velocity of 171, 000 km/h. Pioneer 11 was launched on 6 April 1973 and had very similar mission targets as Pioneer 10. Figure 2 shows the best images of the Galilean moons obtained by both spacecraft. Through tracking of the gravitational perturbation which was acting on the probes, first mass and density estimations could be obtained for the moons. The last signals of the probes were measured in 2003 (Pioneer 10) and 1995 (Pioneer 11). Both probes continue their journeys to leave the Solar System. For more detailed information about early probe missions in the Solar System, see also Siddiqi (2002).

The first high-resolution images of Callisto were obtained from the flybys of the two Voyager probes in 1979 (see Figure 3). The images revealed a highly cratered, inactive and old surface with the Valhalla basin being the largest impact crater. The bright regions were formed during impact events and revealed an icy layer beneath the dark, dusty surface layer (see also section 1.3).

The next important mission was Galileo (1989-2003) which delivered detailed insights into the understanding of surface processes, crater morphologies and the inner structure of Callisto. Galileo started its journey in October 1989 on board of the NASA Space Shuttle Atlantis and performed 8 flybys at Callisto. A high-resolution image of a small region of the Valhalla crater can be seen in Figure 4. Galileo's images revealed regions with a lower crater density than expected (e.g. in the Valhalla region) which can be explained with material moving down the slopes of scarp features due to sublimation processes (Bender et al., 1997). Another possibility may be that the ejecta of the Valhalla impact event covered many of the older craters. Galileo's magnetic field measurements revealed a possible subsurface ocean under Callisto's icy shell (Khurana et al., 1998; Kivelson et al., 1999).

The next large mission studying Callisto will be JUICE (Jupiter Icy moon Explorer). The probe is currently scheduled to start in 2022 and will deliver even more detailed insights into the Jupiter system. It will perform several flybys at Callisto (and Europa) before analysing Ganymede in more detail.

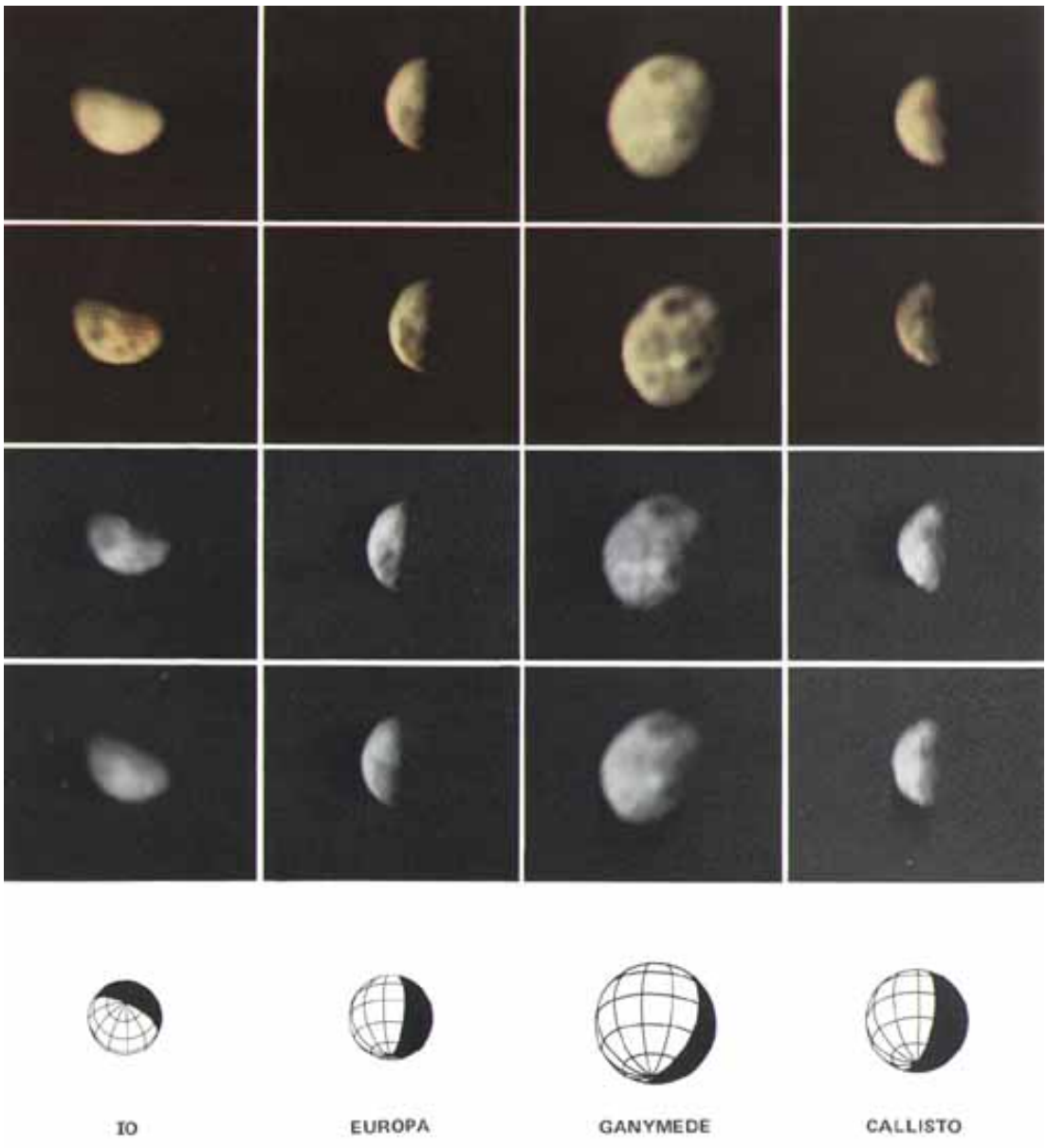

Figure 2: Best images of the four Galilean satellites, obtained by the Pioneer 10 and 11 spacecraft. Each column stands for an individual satellite. The first row shows the colour composite, the second shows the same composite digitally enhanced. The last two panels show the blue and red channels. The bottom row identifies the viewing aspect. (NASA, 1974)

Figure 3: Left: Voyager 1 image of Callisto from a distance of 350,000 km. Features as small as 7 km across can be seen in this image. The bright centre of the Valhalla basin is about 600 km across (Williams and Friedlander, 1979). Right: False colour picture of Callisto by Voyager 2 from a distance of about 1.1 million km. The blue component corresponds to the UV band and shows variations across the surface. Dark blue halos surrounding bright craters imply different material compositions across the surface. The colours were constructed by compositing black and white images taken through the ultraviolet, clear and orange filters (JPL, 1979).

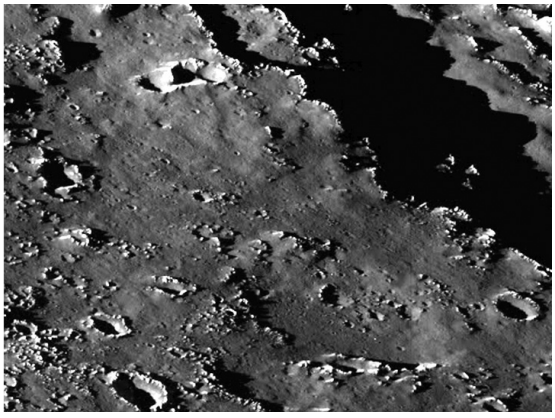

Figure 4: High-resolution image of Callisto's surface within the Valhalla region, covering an area of approximately 33 km^2 (NASA, 1996). The Valhalla region shows a much smaller crater density than the rest of the moon's surface.

1.2 Orbital properties

Table 1 was obtained by JPL's HORIZONS system and summarizes the orbital properties of Callisto's orbit around Jupiter. a is the semi-major axis, e is the numerical eccentricity, i is the inclination with respect to the reference plane, ω is the argument of the periapsis, Ω is the longitude of the ascending node (measured from the node of the reference plane on the ICRF equator) and M is the mean anomaly (at Epoch 1997 Jan. 16.00 TT). n is the longitude rate, P is the sidereal period, P_ω is the argument of periapsis precession period and P_Ω is the longitude of the ascending node precession period. All orbital elements are mean values and are referred to the local Laplace planes.

The sidereal periods of the other Galilean moons (Io, Europa and Ganymede) are 1.77,

a [km]	e [1]	i [°]	ω [°]	Ω [°]	M [°]
1,882,700	0.007	0.192	52.643	298.848	181.408

n [°/day]	P [days]	P_ω [yr]	P_Ω [yr]
21.57	16.69	205.75	338.82

Table 1: Mean orbital parameters and general parameters of Callisto's orbit around Jupiter at Epoch 1997 Jan. 16.00 TT (Jacobson and Brozovic, 2015).

3.55 and 7.16 days respectively. If we compare these periods with Callisto's period of 16.69 days, we notice that Callisto stays in a 7:3 Mean Motion Resonance (MMR) with Ganymede (see Figure 5). For the neighbouring resonances it is true that $9:4 < P_C : P_G < 5:2$, $9:2 < P_C : P_E < 5:1$ and $9:1 < P_C : P_I < 10:1$. Ganymede

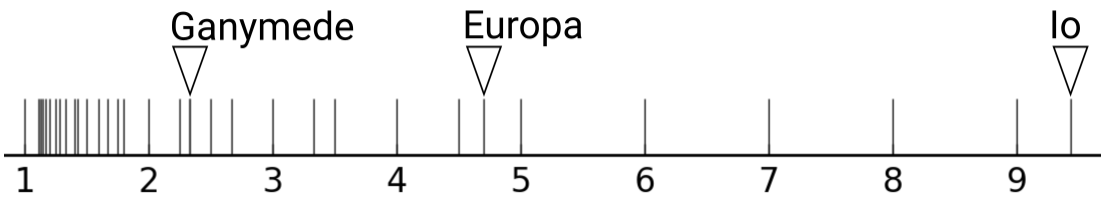

Figure 5: The ratios of the orbital periods $P_C : P_G$, $P_C : P_E$ and $P_C : P_I$ (marked in plot) between Callisto and the other big moons reveal the 7:3 MMR between Callisto and Ganymede. The plot shows all major MMRs between 1:1 and 10:1.

himself stays in a 4:2:1 MMR with Europa and Io. This means that $P_C : P_E \backsimeq 14 : 3$ and $P_C : P_I \backsimeq 28 : 3$.

Callisto's rotational period is equal to her orbital period. This is synonymous with a locked rotation which is quite common for planetary satellites in the Solar System. The locked rotation emerges from tidal forces acting on the moon and slowing it down over time until the rotational and orbital periods are equal.

1.3 Physical properties

Io is the most active Galilean moon with several active volcanoes and therefore she has a very young surface. The other three moons are called *icy moons* because they mostly consist of a mixture between rock and ice. The innermost icy moon Europa may be even habitable for primitive life in her subsurface ocean. Ganymede is the biggest moon in the Solar System, even bigger than the planet Mercury. Callisto, the outermost Galilean moon, is similar to Ganymede, but has very old surface features compared to other massive bodies in the Solar System.

Callisto has a radius of $R = 2,410.3 \pm 1.5\,\mathrm{km}$ (as large as Mercury), what makes her the 3rd biggest moon in the Solar System. With a mean density of $\rho = 1,834.4 \pm 3.4\,\mathrm{kg/m^3}$ (Anderson et al., 2001), one can calculate an approximate mass of $M = 1.076 \cdot 10^{23}\,\mathrm{kg}$. Callisto has a very low albedo of $A = 0.17 \pm 0.02$ (Morrison and Morrison, 1977). The surface is believed to be a mixture between rocky (silicate) and icy components (Helfenstein et al., 1995; Bender et al., 1994). This hypothesis is supported by countless bright crater features which reveal an icy shell beneath a thin and dusty surface layer.

The inner structure of Callisto is not fully understood and there are several suggestions for possible layer arrangements (see Table 2). In contrast to Ganymede, Callisto's gravity data from Galileo showed that she is partly differentiated and hence contains a rocky and icy core (Anderson et al., 1997). The core may be anything between rock/metal and rock/ice and most models propose a rock/ice mantle and an icy shell .

Fluctuations in the magnetic field during Galileo's flybys imply that Callisto shelters a subsurface ocean (Khurana et al., 1998; Kivelson et al., 1999). This result led to the theory of a salty, ammonium-rich ocean with a very low freezing point located under the icy shell.

core [km]	mantle [km]	lower shell [km]	upper shell [km]	Reference
r/i/m: < 1,200	r/i: > 1,000	r/i	i: < 350	Anderson et al. (1998)
r: 887.45	r/i: 1,314.78	w: 72.83	i: 133.79	Thomas and Ghail (2002)
r/i: 1,800-2,000	r/i	w: 120	i/r: 50-150	Nagel et al. (2004)
r/m: < 700	r/i	w: 120-180	i: 135-150	Kuskov and Kronrod (2005)

Table 2: Different models for Callisto's layer arrangement and their thickness. r is rock, i is ice, m is metal and w is water. Note that many bounds are not known precisely and are approximate values. Callisto has a radius of 2,410 km. For purpose of clearness, some layers in this Table were split up into different columns.

1.4 The Valhalla multi-ring basin

Table 3 shows all known large ringed features on Callisto. A longitude of zero degrees is the approximate (±0.4 °) direction of Jupiter and 90 degrees West is the approximate direction of orbital motion around Jupiter.

Crater	*D*[km]	*C lat* [°]	*C lon* [°]	*N lat* [°]	*S lat* [°]	*E lon* [°]	*W lon* [°]
Adlinda	840	-48.5	35.6	-37.8	-56.2	23.4	48.8
Asgard	1,400	32.2	139.9	46.2	12.6	118.4	159.5
Utgard	610	45	134	52.5	39	124	144.5
Valhalla	3,000	14.7	56	53.2	-17	19	83

Table 3: Known impact basins on Callisto with diameters, central coordinates and limiting latitudes and longitudes in each direction (USGS, 2000).

[The following information is mainly adopted from Melosh (1989a).] Craters like Valhalla and Asgard are called *complex craters* (see Figure 8), because they have no simple bowl-shape. This is due to the very last stage of crater formation (modification stage), where rim material collapses and flows back into the recently formed, raw crater (transient crater) and material below the crater is uplifted due to the visco-plastic properties of the material. The uplifting of the visco-plastic material flattens out the crater floor, clearing away the transient bowl-shape. Especially for icy surfaces, melting may play a leading role during the modification stage. The transient crater may also be modified by already existing, liquid water which fills the excavated region and also flattens out the

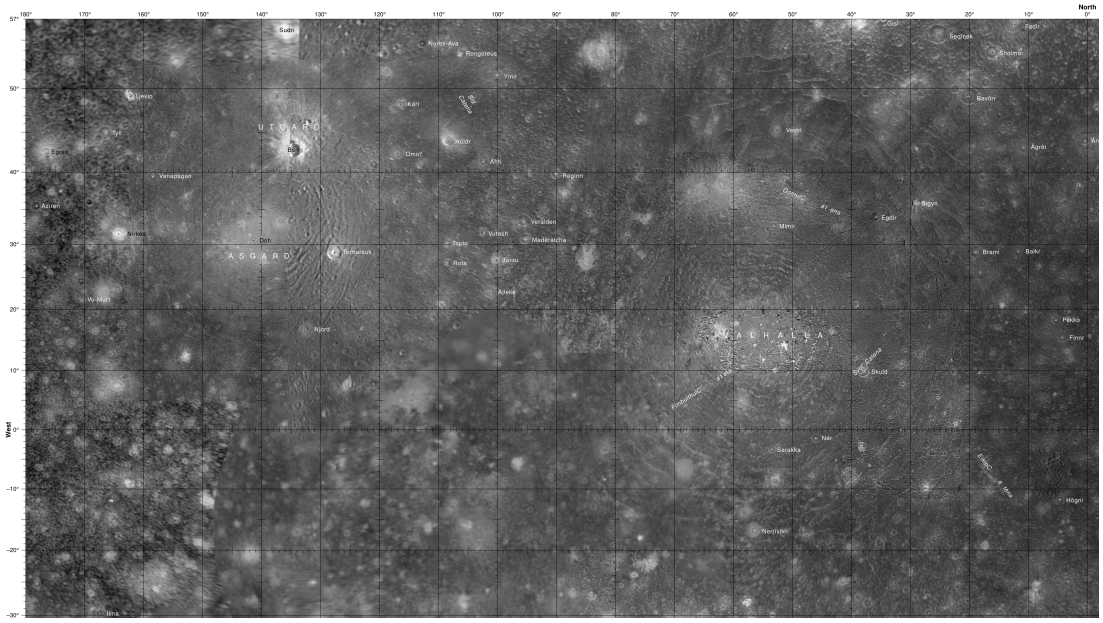

Figure 6: Mosaic of Callisto's largest impact craters obtained by Voyager and Galileo observations (USGS Astrogeology Science Center, 2016). The Valhalla crater fills the right side of the snapshot, Asgard occupies the top left region. The map shows a region of 180×87 degrees on the orbit-facing side, mostly on the northern hemisphere.

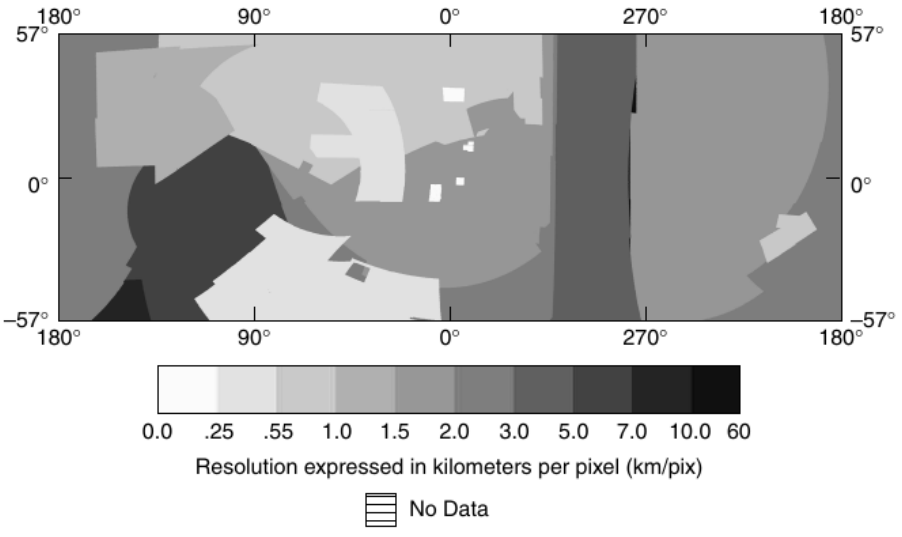

Figure 7: The resolution map reveals that Valhalla and Asgard were observed with resolutions between 3 km/px and 0.25 km/px (USGS Astrogeology Science Center, 2016).

crater floor.

Up to a diameter of about $D = 15\,\mathrm{km}$ the depth/diameter ratio is approximately $1/5$. Larger craters are shallower due to the modification caused by gravity, geologic processes and other processes. Nevertheless, also large craters may have depth/diameter ratios close to $1/5$ during the excavation stage. The surface gravity of a body determines whether a crater is simple or complex. During the modification stage, the crater diameter D of large craters may rise by up to 30-70 percent.

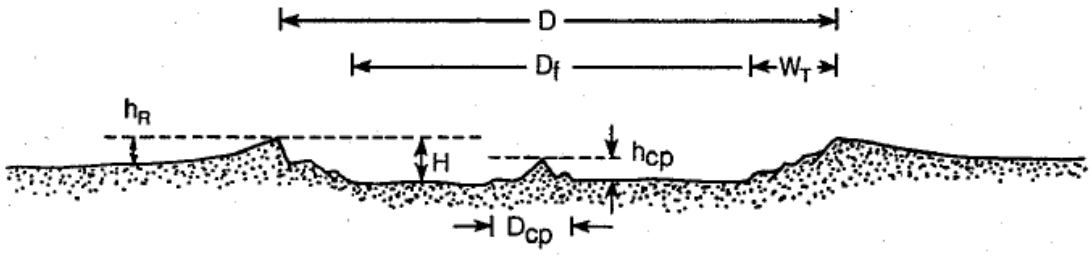

Figure 8: Principal morphometric parameters used to describe complex craters. D is the rim-crest diameter, D_f the diameter of the flat inner floor, W_T is the width of the terrace zone, H is the crater depth, h_R its rim height, D_{cp} is the diameter of the central peak complex and h_{cp} is the height of the central peaks above the crater floor (Melosh, 1989b).

Complex craters often show central peaks or peak-rings within the crater rim. For Callisto, the central peak diameter D_{cp} and maximum central peak formation timescale are given by

$$D_{cp} \simeq 1.45 \cdot e^{0.028 \cdot D} \tag{1}$$

$$t_{cp} \simeq \sqrt{D/g} \tag{2}$$

where D is the rim-crest diameter and $g = 1.236\,\mathrm{m/s^2}$ is the surface gravity of Callisto. Since the transient crater properties D_t and H_t are theoretical quantities, they cannot be obtained by observing the final crater. But if we assume a conserved volume during crater formation, a simple relation between D_t, H_t and D, H can be found:

$$D_t^3 H_t = \frac{5D^3 H}{1 + 6[1 + D_f/D + (D_f/D)^2]^{-1}} \tag{3}$$

The Valhalla crater is not only a complex crater, it is also referred to as a *multi-ring basin*. Not all complex craters are multi-ring basins and vice versa. Multi-ring basins are characterized by concentric, asymmetric, ring-like escarpments which are located at the regions beyond the rim crest of the actual crater (which may be the bright area in Figure 6). At Valhalla, these escarpments are typically a few kilometers high and face outward. The crater density is the same in both the actual crater and the ring-region, indicating they have the same age.

The bright central region measures approximately 600-800 kilometers in diameter which may include both the original crater and the high-albedo ejecta blanket. The innermost 350 kilometers are occupied by a smooth plain which may represent the actual crater. It was argued that there are no peak-ring structures because reasonable amounts of liquids filled the crater during the first stages of its formation (Croft, 1981). We study the crater formation in detail in section 3.4.

A few bright ridges with darker features in-between surround the central region. The ridges are spaced 20-30 kilometers apart and the zone is about 300 kilometers wide. A relatively smooth transition region lies between the ridge zone and the escarpment zone which is about 600 kilometers wide. Scarps can be seen up to 2,000 kilometers away from the centre and they are spaced at distances between 50 and 100 kilometers. In summary, we may distinguish five distinct zones for Valhalla:

- smooth, bright, central region (350 km diameter)
- complete, bright, central region (600-800 km diameter)
- ridge zone (300 km width)
- transition region (200 km width)
- escarpment zone (600 km width)

The overall form of Valhalla appears to be asymmetric with an elongation towards the North-east. Especially the escarpment zone reaches far to the north. This asymmetry could be caused by differences in the geologic structure of Callisto. One may assume that oblique impacts are responsible for this elongation, but research has shown that relatively low impact angles ($\gamma_{imp} \simeq 60\,^{\circ}$) still produce circular craters.

The mechanism for producing multi-ring basins is not fully understood and there are different ideas:

- The Volcanic Modification Hypothesis suggests that lava which lies beneath the original crater modifies the said crater at later times. The lava penetrates the crater floor along ring faults and produces rings (Hartmann and Yale, 1968).

- The Megaterrace Hypothesis suggests that a very large terrace forms in analogy to ordinary terraces which can be found at complex craters. The large terrace origins from weakened material in the outskirts of the crater (Head, 1977).

- The Nested Crater Hypothesis suggests that ring-like structures are formed by the influence of different material layers. As the crater floor is uplifted the ledges which are present in the transient crater are tilted outward and produce rings (Hodges and Wilhelms, 1978).

- The Ring Tectonic Hypothesis suggests that faults in the lithosphere are produced under the influence of a fluid asthenosphere (Baldwin, 1972; Melosh and McKinnon, 1978). A more detailed description is given in the text.

Callisto shows no evidence of volcanic activity and the Nested Crater Hypothesis may not apply due to the same crater density in both the crater and the ring-region. The Megaterrace Hypothesis as well as the Ring Tectonic Hypothesis may both be valid explanations, but for this thesis we focus on the Ring Tectonic Hypothesis. For this hypothesis, a *brittle* lithosphere and a *liquid* asthenosphere near the surface are needed. On Callisto, the lithosphere is the outer icy/rocky shell, while the asthenosphere could be a more plastic/liquid material like Ice II or water. We distinguish three possible types for crater formation in the context of the Ring Tectonic Hypothesis (see also Figure 9):

1. If the lithosphere is much thicker than the transient crater depth, nothing special happens. A simple or a complex crater is created depending on the crater size.

2. If the transient crater depth is larger than the thickness of the lithosphere, at least one ring may form in the outskirts of the crater due to inward flowing asthenosphere-material which is filling the crater bowl. The inward flowing material causes an

inward drag on the lithosphere and - if strong enough - produces extension fractures (scarps) in the lithosphere. The low-viscosity asthenosphere must lie on a higher-viscosity layer (e.g. rock, Ice I or Ice III), otherwise no extensional stresses can be produced.

3. If the transient crater depth is much larger than the lithosphere thickness, additional radial fractures may form due to waves crossing the interior of the body and pushing the lithosphere upward and outward.

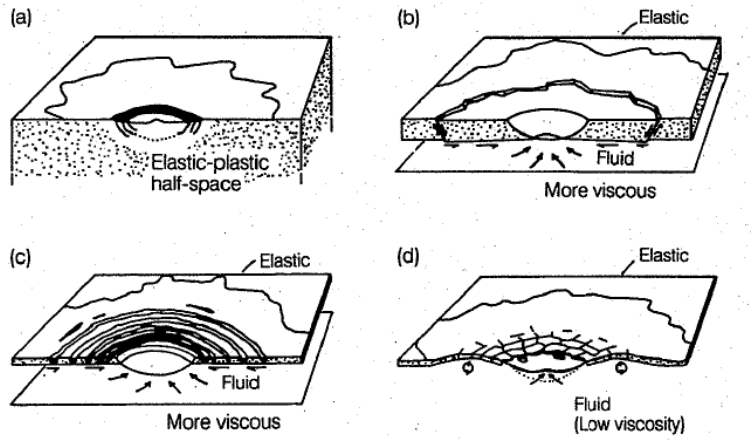

Figure 9: Scenarios for the ring tectonic hypothesis with a) thick b) thinner c) thin d) very thin lithospheres. a) corresponds to type 1, b) and c) to type 2 and d) to type 3 (Melosh, 1989c).

The scarps cannot form too close from the crater rim because of too small extensional forces. On the other hand, they cannot form too far where the lithosphere can easily resist the extensional forces. The lithosphere must be relatively brittle which is the case for Jupiter's icy satellites. Since Valhalla has a very distinct scarp-zone, the transient crater should be deeper than the thickness of the lithosphere (type 2). Nevertheless, Valhalla does not show radial features (type 3) which implies a certain thickness of the lithosphere. Secular cooling may have thickened Callisto's lithosphere, thus suppressing the formation of type 3 craters.

2 N-body simulations

The impact velocity v_{imp} and the impact angle γ_{imp} are two very important parameters when it comes to impact events. The velocity is even more important than the mass of the impactor because the kinetic energy which is transferred to the target during the impact is proportional to the square of the velocity but only linearly dependent on the mass:

$$E_{kin} = \frac{m v_{imp}^2}{2} \tag{4}$$

The gravitational acceleration of Jupiter before the impact is not negligible if we want to find plausible v_{imp}. Therefore it can not be assumed to be the escape velocity (v_{esc}) of the target. In order to use appropriate v_{imp} for the SPH simulations in section 3, we investigated this topic with n-body simulations.

2.1 The code

2.1.1 Operating modes

The algorithm operates in two modi. The first one (*normal mode*) focuses on the acceleration of the particles by Jupiter while the second one (*moon mode*) focuses on the moon impacts. We included both Ganymede and Callisto in our simulations to compare the results.

All simulations start in normal mode, where particles are spawned at the edge of Jupiter's Hill sphere and are sent into the inner Jupiter System (see section 2.2 for further information). If a particle enters the Hill sphere of one of the moons, a measurement is taken. The same is true for the closest approach and for exiting the Hill sphere again.

In general, one would assume a vast number of close encounters in comparison to actual collisions with a moon. Therefore, we use a computational trick to be able to construct a collision for every close encounter event: When entering the Hill sphere, all positions and velocities of all objects in the simulation are saved. If no collision happened (which is true for almost all simulations in normal mode), the algorithm switches to the moon mode, where new simulation runs are initialized. For the initial simulation setup in moon mode, the information of the corresponding normal mode simulation is used. The posi-

tions and velocities of the massive bodies remain the same. Also the velocity vector of the particle which entered the Hill sphere remains unchanged. Only the position of the particle changes in such a way that it was randomly put at other positions on the edge of the corresponding moon's Hill sphere. The system then evolves and the particle is tested for a collision. If no collision happens, the simulation is reset and another random, initial position is initialized. This process repeats until a collision happens and a measurement can be taken. The algorithm then switches back to normal mode and continues further runs.

Since Jupiter's Hill sphere is by magnitudes larger than the Hill spheres of the moons (see Figure 10), we can argue that the particle could have had a very similar trajectory (and hence acceleration) before entering the Hill sphere of a moon. Therefore the particle could have entered the moon's Hill sphere at any position (on the particle-facing side) with only small variations of the initial conditions at the edge of Jupiter's Hill sphere. We intentionally induce a systematic error to achieve a very high collision rate and thus be able to analyse the results in a statistical manner. We choose this kind of approach because we want to find typical impact velocities rather than highly accurate ones. Moreover, one does not know accurate initial conditions either, what makes an estimation of impact velocities very difficult in any case.

To sum up, we assume that the particle undergoes the same acceleration (simulated in normal mode) until entering the Hill sphere and colliding with one of the moons (simulated in moon mode). We designed the code to be very efficient and yield high collision rates at the cost of a systematic error.

2.1.2 Integration method

Our n-body code is written in Fortran95 and uses the Runge-Kutta Cash-Karp (RKCK) method with embedded adaptive stepsize control (Cash and Karp, 1990). We use the template code given in the Numerical Recipes to implement the method (Press et al., 1993). The following pseudo code describes how a step is taken using the RKCK method:

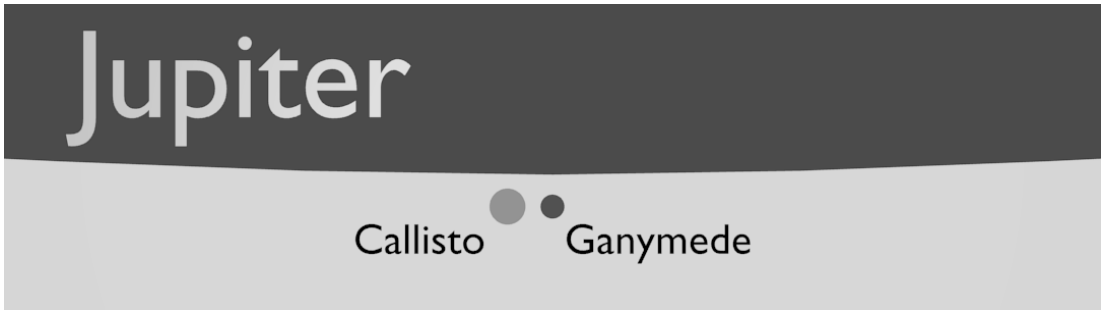

Figure 10: Jupiter's Hill sphere ($r_{Hill} = 0.338$ AU) is approximately 1,600 and 1,000 times larger than those of Ganymede ($r_{Hill} = 0.0002$ AU) and Callisto ($r_{Hill} = 0.0003$ AU). This difference in size is our argument to use the computational trick in order to gain a very high collision rate.

```
1  newton(y, K1)
2  newton(y + h * a1*K1, K2)
3  newton(y + h * (b1*K1 + b2*K2), K3)
4  newton(y + h * (c1*K1 + c2*K2 + c3*K3), K4)
5  newton(y + h * (d1*K1 + d2*K2 + d3*K3 + d4*K4), K5)
6  newton(y + h * (e1*K1 + e2*K2 + e3*K3 + e4*K4 + e5*K5), K6)
7  y4 = y + h * (f1*K1 + f2*K3 + f3*K4 + f4*K5)
8  y5 = y + h * (f5*K1 + f6*K3 + f7*K4 + f8*K5 + f9*K6)
9
10 error = y5 - y4
11 if error < tolerance:
12   accept step: y(t+h) = y5
13 else:
14   reject step: reduce h and recalculate y4 and y5
```

y contains the 3-dimensional positions and velocities of all objects in the system. The function *newton* calculates the accelerations acting between the objects and stores the results along with the corresponding velocities in the given K. With each K, a specific set of help-points can be derived during the step (e.g. $y + h \cdot a1 \cdot K1$, see figure 11). Note that each new K depends on all previously derived ones (e.g. $K4$ depends on $K3$, $K2$ and $K1$).

The lowercase letters $a1$ to $f9$ are real numbers and act as weights for the corresponding K. The 4th order solution $y4$ and the 5th order solution $y5$ can then be derived using the calculated K values. Note that $K2$ is not needed for the solutions. Assuming $y5$ to be the true solution (which is never fulfilled, but a better approximation than $y4$), the two solutions are compared and yield absolute errors for the positions and velocities. If the error is larger than a given tolerance, the step is rejected and the whole procedure has to be repeated with a smaller stepsize h. If the error fulfills being smaller than the tolerance (see section 2.1.3), the step is accepted and the 5th order solution is used for the next step. Since both the lower and higher order solution can be computed with the same K values,

Figure 11: Starting from $y(t)$, the RKCK method constructs help-points (dotted circles) to derive the 4th and 5th order solutions for $y(t + h)$. If the error (indicated by the line) is smaller than a given tolerance, the step is accepted.

the RKCK method shows a quite good performance when using adaptive time stepping. This performance is useful to produce enough measurements for finding typical impact velocities and impact angles (see also section 2.3.1). On the other side, there is also a major disadvantage using the RKCK scheme: In general, Runge-Kutta methods do not conserve the momentum of a system. This means that with each step, a small amount of momentum gets lost or produced by using this numerical scheme. Nevertheless, we concluded to use the RKCK method because:

- We aimed to find typical impact velocities and angles rather than highly exact values.
- The initial conditions for particles intersecting the Jupiter system remain unknown and can only be approximated roughly (see also section 2.2.2).
- The intended systematic error is much larger than the error caused by loosing momentum through the integration method (see also sections 2.1.3 and 2.1.1).

The typical simulation time in normal mode is 1.4 years at maximum, depending on the trajectory of the particle. Within these 1.4 years, every possible combination of the initial positions and velocities allows a flyby at Jupiter and two intersections with the orbits of both moons. The average simulation time in moon mode is between 15 and 130 minutes, depending mostly on the relative velocity between the particle and the respective moon. The typical number of steps for simulations in normal mode (moon mode) are 81k (400) and typical stepsizes lie between 45 minutes and 5 minutes (5 minutes and 5 seconds).

2.1.3 Acurracy

The relative error tolerance is set to $\epsilon = 10^{-11}$ and the absolute error tolerance is $tol_x = 0.1 \cdot \epsilon \cdot mean(x_{rel})$ for the positions and $tol_v = \epsilon \cdot mean(v_{rel})$ for the velocities. A safety factor of 0.1 is used for the positions because it approximately reflects the median value of the relative distances during the simulations. Since the median value is computationally more expensive to calculate, this empirical factor is introduced. The average, relative distances (velocities) are approximately 3.5 AU (11 km/s) which yield absolute error tolerances of about of about 0.5 m (10^{-7} m/s) for each step. A typical simulation run has about 81k steps in normal mode. Since the errors for each step sum up, the total error for a typical simulation is about 121.5 km (0.009 m/s). The numerical errors are therefore negligible in comparison to the intentional systematic error we get using the computational trick mentioned in section 2.1.1. The intentional error can be up to one Hill radius of the respective moon (see also Figure 10). However, we set up an additional stepsize limit to avoid overshooting in case of collisions and assure even higher accuracy at impact events:

$$h_{max} = 0.01 \cdot \frac{d_{min}}{v_{rel}} \tag{5}$$

d_{min} is the minimum distance between a particle and a moon and v_{rel} their corresponding relative velocity. A particle in vicinity of the moon is thus allowed to travel up to 1% of the distance to the moon at each step. The particle is also allowed to enter the surface of the moon by up to 1% of its radius. With this additional constraint, we are able to measure the impact latitude on the moon with an accuracy of 1% of the respective moon's radius.

Since the impact longitude is by far the bigger problem (because the position on the orbit around Jupiter at the time of the impact remains unknown), an exact measurement would not yield valuable information. Therefore, we only distinguish between four sectors for the longitude which origin from the four possible combinations of prograde and retrograde impacts and whether the impactor already had its closest approach to Jupiter.

2.2 Object setup

It is crucial to choose proper constraints for initial orbits of test particles intersecting the Jupiter system. For purposes of simplicity, we focus on particle-orbits with orbits similar to Jupiter's orbit. Therefore, the intersection-velocities are typically low in comparison with objects like comets or asteroids from the Centaur family which usually have highly eccentric and/or highly inclined orbits. Our findings for typical intersection velocities are discussed in the following sections.

2.2.1 Massive particles

Four massive bodies are used for the simulations: The Sun, Jupiter, Ganymede and Callisto. We assume that the moon formation has already finished at the time of the impact and that the moons of Jupiter as well as Jupiter himself are already at their current positions in semi-major axis. The orbital -and physical properties of the Jupiter System were obtained from NASA's Horizon system (Jacobson and Brozovic, 2015). The small inclinations of Jupiter ($i = 1.304\,^\circ$), Ganymede ($i = 0.177\,^\circ$) and Callisto ($i = 0.192\,^\circ$) were neglected. We also neglect the atmospheres of the moons because they have no significant influence on the momentum of the particles. A thin oxygen atmosphere with a surface pressure of about $P = 10^{-6}$ bar was measured at Ganymede (Carlson et al., 1973). The Galileo probe revealed an extremely thin carbon dioxide atmosphere with a surface pressure of about $P = 7.5 \cdot 10^{-12}$ bar at Callisto (Carlson, 1999).

2.2.2 Test particles

The test particles are put randomly at the edge (between 95% and 100%) of Jupiter‘s Hill sphere:

$$\begin{pmatrix} x \\ y \\ z \end{pmatrix} = \begin{pmatrix} a_1 \cdot rand_1 \\ a_2 \cdot rand_2 \\ a_3 \cdot rand_3 \end{pmatrix} \cdot r_{Hill,♃} \tag{6}$$

where the $rand_{1,2,3}$ are random numbers between 0.95 and 1 and $a_{1,2,3}$ are randomly chosen integers either being +1 or −1. Jupiter's Hill radius is given by equation 7 and yields $r_{Hill,♃} \approx 0.338$ AU.

$$r_{Hill,♃} \approx a_♃(1 - \epsilon_♃)\sqrt[3]{\frac{m_♃}{3M_\odot}} \tag{7}$$

For the estimation of the initial, random velocities of the test particles, the following constraints are made:

- All particles have initial eccentricities ϵ between 0 and 0.1.
- All particles have initial inclinations i between 0 ° and 10 °.
- In order to avoid a large numerical overhead and performance issues, all velocity vectors initially have to point towards the inner Jupiter system with a maximum angle of $y = 15$ ° between $\overrightarrow{v_{rel}}$ and $\overrightarrow{d_{rel}}$ (between a particle and Jupiter). See the draft in Figure 12 for further information.

Because of limited computational power, we are not able to explore the full parameter space with our method. For the sake of this thesis, this fact may not be critical to achieve our main aim of finding rough constraints for typical impact velocities and masses of the impactor to reconstruct the Valhalla crater. However, using similar orbits to Jupiter may also cause problems regarding orbital resonances: The particles are close to the 1:1 MMR with Jupiter which may result in natural limitations to possible intersection geometries. This problem is beyond the aims of this thesis and we did not analyse likely intersection scenarios caused by resonances. However, more sophisticated studies with advanced n-body algorithms are already in progress (Winter et al. (2017) in prep. EPSC 2017).

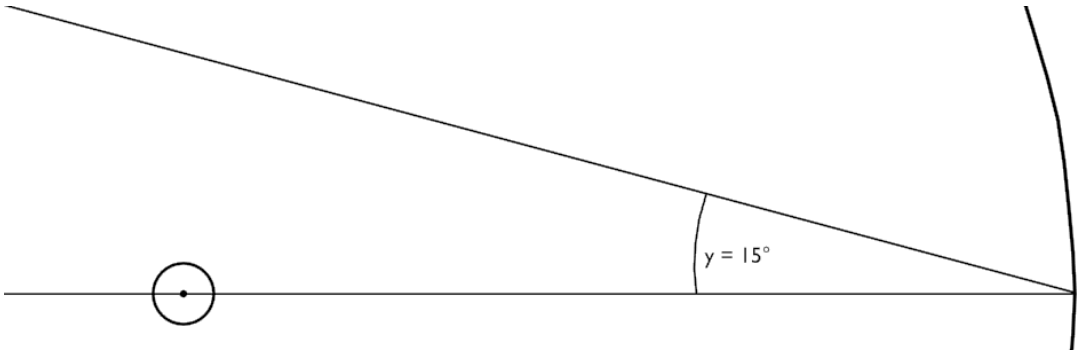

Figure 12: The initial, relative velocity vector v_{rel} of the particle has to point towards the inner Jupiter system with a tolerance of $y = 15\,°$. This may cause unwanted, systematic errors resulting in slightly higher impact velocities. The circle at the left corresponds to Callisto's orbit around Jupiter and the curve at the right is the edge of Jupiter's Hill sphere.

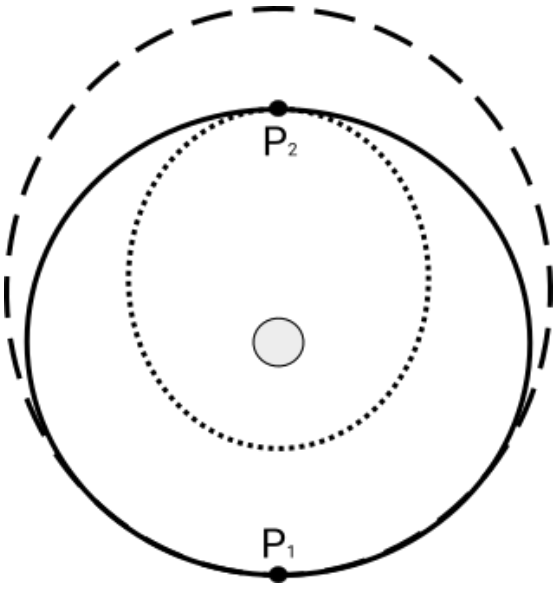

Figure 13: Draft for possible special orbits of test particles with $\epsilon = 0.1$. The solid line corresponds to Jupiter's orbit. Collisions can only occur in P_2 or in P_1. All other orbits in-between the dotted and the dashed one intersect Jupiter's orbit twice.

The lower bounds for the relative velocities at the edge of Jupiter's Hill sphere are zero. This corresponds to a particle with the exact same orbital parameters as Jupiter.
The upper bound for the maximum, relative, orbital velocity was estimated using the *Vis-Viva equation* (equation 8). $\mu = GM_\odot$, r is the actual distance from the Sun and a is the semi-major axis of the object.

$$v_{orbit} = \sqrt{\mu\left(\frac{2}{r} - \frac{1}{a}\right)} \tag{8}$$

For the calculation of the maximum, relative, orbital component, the inclination was neglected. Using equation 8 for Jupiter yields an orbital velocity of $v_{♃} = 13.06\,\mathrm{km/s}$. The orbital velocity of a test particle can be calculated setting $r = a_{♃} = 5.2\,\mathrm{AU}$ and $a = r_{perihelion}/(1-\epsilon) = 5.78\,\mathrm{AU}$ and yields $v_p = 13.69\,\mathrm{km/s}$. $|v_{♃} - v_p|$ yields a relative velocity of $v_{rel} = 0.64\,\mathrm{km/s}$. This corresponds to the red case in Figure 13. The blue case in Figure 13 can be treated similarly: By using $r = a_{♃} = 5.2\,\mathrm{AU}$ and with $a = r_{aphelion}/(1+\epsilon) = 4.73\,\mathrm{AU}$ the relative velocity is $v_{rel} = 0.67\,\mathrm{km/s}$. Note that for this case, the particle lies in the apoapsis at the intersection and therefore has a smaller orbital velocity (12.387 km/s) than Jupiter (13.057 km/s). Considering both cases, the maximum relative, orbital velocity component is set to $v_{rel} = 0.67\,\mathrm{km/s}$.
The maximum, radial velocity was estimated by intersecting a circle (Jupiter's orbit) with an ellipse (particle's orbit) with $\epsilon = 0.1$. Note that Jupiter has a very small eccentricity of $\epsilon = 0.05$. It is neglected because the particles are put at the edge of Jupiter's Hill sphere at the beginning of the simulations and Jupiter's Hill sphere covers the whole region between the perihelion and the aphelion. The semi-major axis a_p of the particle is set to the mean value of the apsides for the cases red and blue in Figure 13. For the semi-minor axis it is true that $b_p = a_p\sqrt{1-\epsilon^2}$. The equations for the elliptic and circular obits are then:

$$\frac{x^2}{a_p^2} + \frac{y^2}{b_p^2} = 1 \tag{9}$$

$$x^2 + y^2 = a_{♃}^2 \tag{10}$$

One can intersect these two orbits and calculate the slopes at the intersection. The slopes can be used to find the angle between the orbits. The angle was found to be $\alpha = 0.29\,^\circ$.

Since the eccentricity is very low, the intersection angle is very small. We obtain a maximum, relative, radial velocity component of $v_{rel} = 65\,\mathrm{m/s}$.
The maximum relative, vertical component for an object with $a_p = a_{\varsigma_+}$ and $i = 10^\circ$ can be calculated with equation 11.

$$v_{rel,vertical} = v_{orbit} \cdot 2sin(i/2) \tag{11}$$

This equation has to be seen as an approximation because the velocity vectors point to the direction $90^\circ + i/2 = 95^\circ$ and not perpendicular to the orbital plane of Jupiter. Nevertheless, it yields reliable results for relatively small inclinations. The maximum, relative, vertical velocity component is thus $v_{rel} = 4.534\,\mathrm{km/s}$.
For the actual simulations, each particle is assigned a randomly chosen velocity

$$\begin{pmatrix} v_{rel,orbital} \\ v_{rel,radial} \\ v_{rel,vertical} \end{pmatrix} = \begin{pmatrix} a_1 \cdot rand_1 \\ a_2 \cdot rand_2 \\ a_3 \cdot rand_3 \end{pmatrix} \cdot \begin{pmatrix} 670 \\ 65 \\ 4,534 \end{pmatrix} m/s \tag{12}$$

where $rand_{1,2,3}$ are random numbers between 0 and 1 and $a_{1,2,3}$ are, again, randomly chosen integers either being $+1$ or -1.

2.3 Results and data analysis

In this section we summarize and analyse the main results of the n-body simulations. The simulations were performed on 8 individual cores, each using the identical input parameters described above. The total simulation time was 1 week per core.

2.3.1 Raw data

A total number of 68,939 measurements were taken during the simulations. At each of the following events, a measurements was taken:

- particle entering the Hill sphere of a moon
- particle colliding with a moon
- particle having its closest approach to a moon

- particle exiting the Hill sphere of a moon

We may refer to these four families of events with the numbers 1 (entering), 2 (colliding), 3 (closest approach) and 4 (exiting). Moreover, we may split up the data corresponding either to Ganymede or Callisto. Since Callisto's Hill radius is larger in comparison to Ganymede's, about twice as many events were measured for Callisto. The exact numbers of events for each event family and each moon are summarized in Table 4.

	event 1	event 2	event 3	event 4	sum
Ganymede	5,574	5,574	5,535	5,535	22,218
Callisto	11,703	11,660	11,679	11,679	46,721

Table 4: Number of events by moon and event type.

As stated in section 2.1.1, we are able to construct a collision for almost every event 1. This resulted in approximately one out of four events being a collision. However, there are minor differences between the number of events for Callisto (Ganymede): 24 (39) collisions were detected in normal mode and the intended systematic error by using the moon mode (discussed in section 2.1.1) did not apply. The measurements for those collisions are presented in Table 10 and Table 11 in the Appendix. Events 3 and 4 could not be measured for those cases. For 43 (0) simulations, no collision could be measured at all because the velocity vector of the particle was not compatible with any initial position in moon mode. Therefore, event 1 for Callisto is larger by 43 in comparison to event 2.
Each measurement contains the following information with the corresponding units in square brackets:

- index of the moon [1]
- event type [1]
- retrograde or prograde flag (in the context of the moon's orbit around Jupiter) [1]
- closest approach flag (to Jupiter) [1]
- time of measurement [s]

- relative velocity between the particle and the moon [m/s]
- angle between the relative distance vector and the relative velocity vector [°]
- closest distance to the moon [m]
- z-coordinate of the particle (to reproduce the impact latitude) [m]
- stepsize at measurement [s]

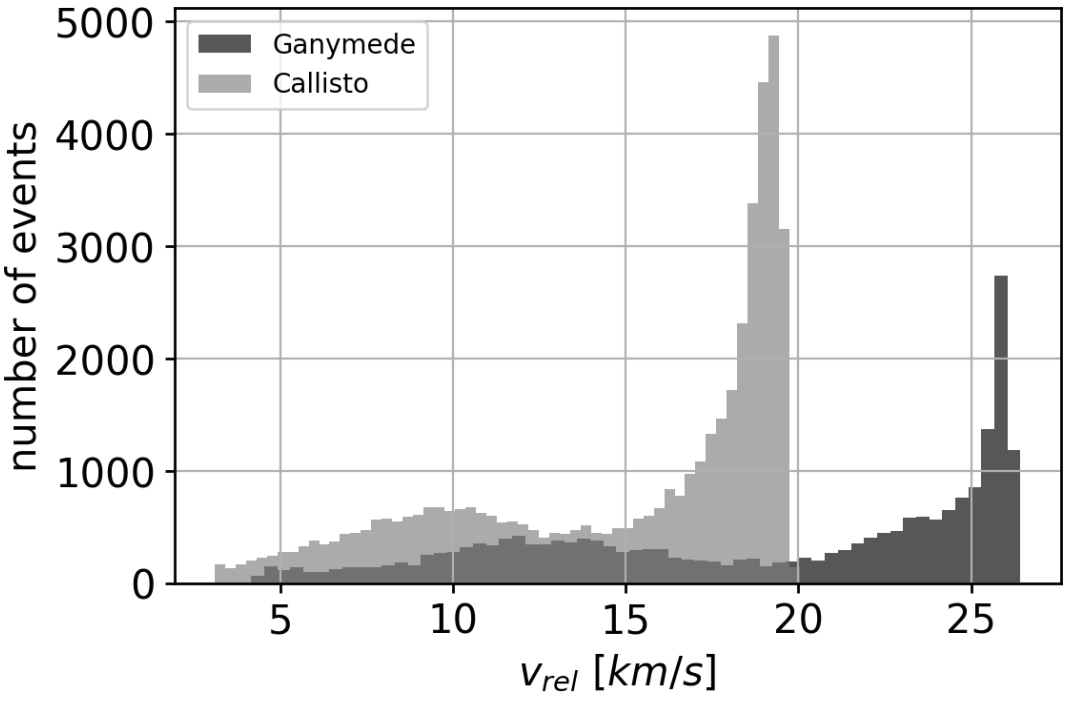

Figure 14: Distribution of all events in the velocity space. v_{rel} corresponds to the relative velocity between the particle and the corresponding moon. $v_{rel} \equiv v_{imp}$ for impact events.

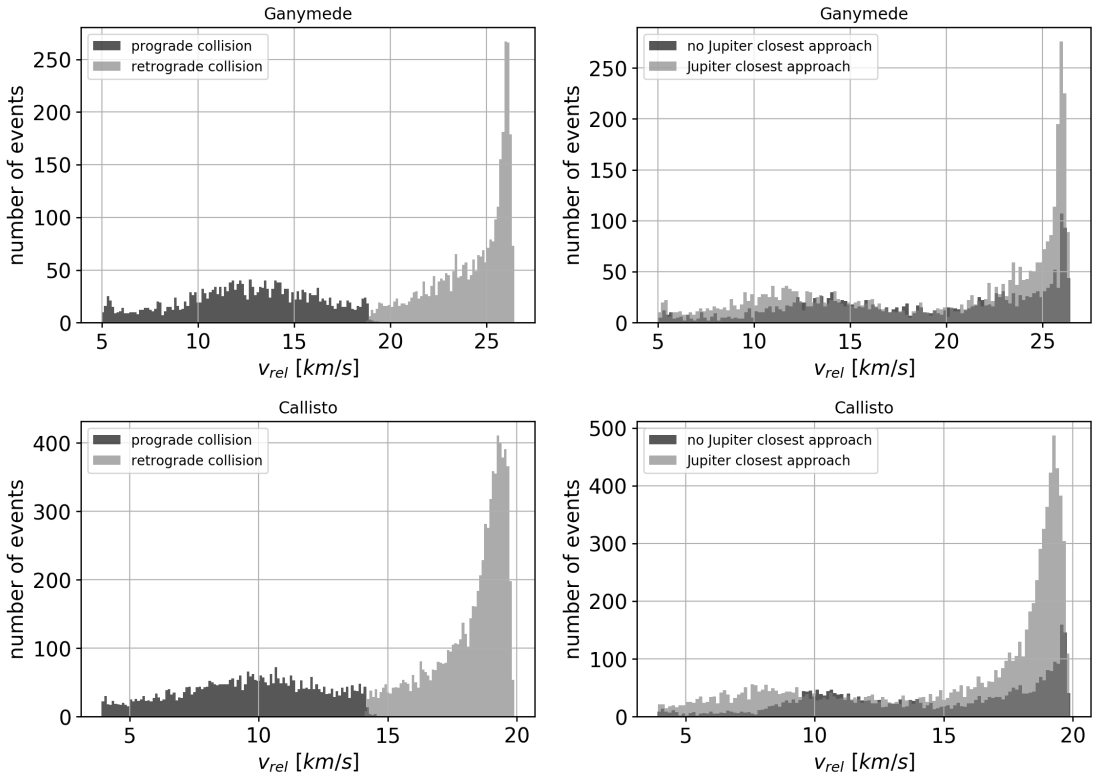

Figure 15: Left column: A clear separation of low-velocity and high-velocity impacts can be seen. This separation originates from prograde and retrograde collisions with respect to the orbital motion of the moons. Right column: Due to the influence of the Sun, particles are significantly scattered into Jupiter's orbital plane during the flyby. This results in statistically more particles colliding with the moons. Note that the axis ranges for Ganymede and Callisto are different.

2.3.2 Impact velocities

Figure 14 summarizes the raw data of all measurements and Figure 15 shows more details about impact velocities with differently sorted data. Following interpretations can be extracted from these results:

There is a clear separation between low-velocity impacts happening in the same direction as the orbital motion (prograde) and high-velocity impacts happening against the orbital motion (retrograde) of the moons. This means that the gravitational attraction of the moons only plays a minor role when it comes to the additional acceleration of the particles.

The general shape of the low-velocity region is broader in comparison to the high-velocity region because of the geometry of the problem: If particles are coming from the front, they must have entered the Hill sphere of the moon in a tighter region compared to particles coming from behind. This effect also seems to shift the high-velocity peak a bit to the right.

The impact velocity at the peak of the low-velocity (high-velocity) region is $v_{imp} = 12.65\,\mathrm{km/s}$ ($v_{imp} = 25.91\,\mathrm{km/s}$) for Ganymede and $v_{imp} = 10.62\,\mathrm{km/s}$ ($v_{imp} = 19.22\,\mathrm{km/s}$) for Callisto with the corresponding numbers of events $n = 41$ ($n = 267$) and $n = 72$ ($n = 411$). We can compare the height of the low-velocity and high-velocity peaks to find the ratios $\eta = 6.5$ for Ganymede and $\eta = 5.7$ for Callisto. Ganymede's slope seems to be a bit steeper than Callistos', what could also be due to the geometric effect. The high-velocity region for Ganymede is narrower than for Callisto which results in a larger difference between the height of the peaks.

The distances in velocity between the two major peaks are approximately reflecting the orbital velocities of the moons ($v_{orb,Gan} = 10.9\,\mathrm{km/s}$ and $v_{orb,Cal} = 8.2\,\mathrm{km/s}$). With increased distance from Jupiter the gap between the two peaks vanishes. On the other hand, this effect may give rise to forbidden regions for Europa and Io.

For both Ganymede and Callisto there is a sharp cut-off on the right side which strictly constrains the upper limit for possible impact velocities (using the initial constraints discussed in section 2.2.2). The cut-off may originate from the combination of initial conditions, the orbital velocity of the moons and possible geometries of impact trajectories. However, objects like comets and asteroids of the Centaur family may be located to the right of this cut-off.

For Ganymede, there is a third, small peak at the lower end of the low-velocity region. This peak may be caused by the moon's acceleration of ultra-low velocity particles within Ganymede's Hill sphere. The peak may also be present for Callisto, but the statistical fluctuations of the data do not allow for a significant statement.

For intermediate velocities (Ganymede: $12\,\mathrm{km/s} < v_{rel} < 22\,\mathrm{km/s}$, Callisto: $9\,\mathrm{km/s} < v_{rel} < 14\,\mathrm{km/s}$), it seems to be quite irrelevant whether the particle already had its closest approach to Jupiter before the collision.

In contrast to the intermediate-velocity regions there is a strong effect at the high-velocity

end (Ganymede: $22\,\mathrm{km/s} < v_{rel}$, Callisto: $14\,\mathrm{km/s} < v_{rel}$). Particles which already had their closest approach to Jupiter are dominating this region. This can be explained with drastic changes in inclination of highly inclined particles during their Jupiter flyby, forcing them into the orbital plane of Jupiter and his moons. Comparing the numbers in Table 5, this effect is stronger by a factor of 1.4 for Callisto than for Ganymede because the interaction period (with Jupiter) before the impact is longer. This implies that the Sun has a major influence on the moon's impact rates.

Variations also appear for the low-velocity regions of both moons (Ganymede: $v_{rel} < 12\,\mathrm{km/s}$, Callisto: $v_{rel} < 9\,\mathrm{km/s}$). They also seem to be significantly more populated by collisions of particles which already had their closest approach to Jupiter. Since the particles are gravitationally influenced by the moons for a longer period, there might be a dependence on the velocity. On the other hand, the effect disappears again at the lowest velocities, what disadvantages this explanation. Another possibility might be (in agreement with the high-velocity regions) the influence of the Sun and Jupiter during the movement within the moon's Hill sphere. This would also explain the stronger signal for Callisto than for Ganymede.

	prograde	retrograde	no periapsis	periapsis
Ganymede	2,412	3,162	2,049	3,525
Callisto	4,141	7,519	3,399	8,261

Table 5: The attributes *retrograde* and *periapsis* are favoured in comparison to *prograde* and *no periapsis*. See text for details.

Table 5 shows the number of collision measurements for each subset in Figure 15. The ratio between retrograde and prograde events is $\eta = 1.3$ ($\eta = 1.8$) for Ganymede (Callisto). This explains - in combination with the narrower region caused by geometric effects - that the high-velocity peaks in Figure 15 are much higher than the low-velocity peaks. The results for the closest approaches to Jupiter are similar: It is more likely that a particle already encountered Jupiter by a factor of $\eta = 1.7$ ($\eta = 2.4$). We can now compare

the results of Ganymede and Callisto by comparing the ratios of the ratios

$$\frac{\text{retrograde} \;/\; \text{prograde}}{\text{periapsis} \;/\; \text{noperiapsis}} \tag{13}$$

which yields 1.32 (1.34) for Ganymede (Callisto). This simple comparison implies that there might be a tight relation between the four attributes and both moons, favouring the attributes *retrograde* and *periapsis*.

2.3.3 Analytic estimation of impact velocities

The escape velocities of Jupiter, Ganymede and Callisto can be derived using equation 14, where r corresponds to the distance from the centre of the body and M being the total mass of the body.

$$v_{esc} = \sqrt{\frac{2GM}{r}} \tag{14}$$

Using the respective masses and radii of Jupiter, Ganymede and Callisto, one gets $v_{esc,♃} = 59.5\,\mathrm{km/s}$, $v_{esc,Gan} = 2.7\,\mathrm{km/s}$ and $v_{esc,Cal} = 2.4\,\mathrm{km/s}$. If we now use Jupiter's mass for M and the semi-major axes of the moons for r, we get typical particle velocities at the position of the moons orbits: $v_{esc,Gan,orb} = 15.4\,\mathrm{km/s}$, $v_{esc,Cal,orb} = 11.6\,\mathrm{km/s}$. The orbital velocities of both moons are given by $v_{orb,Gan} = 10.9\,\mathrm{km/s}$ and $v_{orb,Cal} = 8.2\,\mathrm{km/s}$. We can now estimate the highest and lowest possible impact velocities for both moons:

$$v_{imp,max,moon} = v_{esc,moon,orb} + v_{orb,moon} + v_{esc,moon} \tag{15}$$

$$v_{imp,min,moon} = v_{esc,moon,orb} - v_{orb,moon} + v_{esc,moon} \tag{16}$$

Using the corresponding values for both moons, one gets: $v_{imp,max,Gan} = 29.0\,\mathrm{km/s}$, $v_{imp,min,Gan} = 7.2\,\mathrm{km/s}$, $v_{imp,max,Cal} = 22.2\,\mathrm{km/s}$, and $v_{imp,min,Cal} = 5.8\,\mathrm{km/s}$. Comparing these numbers with the simulation outcomes, the analytic estimation overestimates the impact velocities by about 2 km/s for both moons.

2.3.4 Comparison: Callisto impacts and closest approaches

Since it is by far more likely for a particle to miss its target rather than colliding with it, we briefly discuss the differences between the impact events and closest approach events. Figure 16 shows the ratio between the impact velocity (in moon mode) and the velocity at the corresponding closest approach (in normal mode) depending on the closest approach distance. One can see that the ratio converges to unity when the particle passes Callisto very close. The highest differences (with a maximum of $\sigma = 1.259$) appear, as expected, at the highest distances because the corresponding systematic error is also high. The mean ratio is $\sigma = 1.021$. Thus, one can use the close-encounter data for estimating typical impact velocities with the following empirical equations:

$$v_{imp,max} = 1.259 \cdot v_{closest\ approach} \tag{17}$$

$$v_{imp,mean} = 1.021 \cdot v_{closest\ approach} \tag{18}$$

The errors are not only caused by shifting the particles along the edge of Callisto's Hill sphere, but they also experience slightly different accelerations.

2.3.5 Impact angles

Figure 17 shows the results of the impact angles for Callisto. As expected from geometric thoughts (Gilbert, 1893), the angles show a parabola-like distribution with a single peak around $< \gamma_{imp} > = 45\,^{\circ}$. The simulations yield a mean value of $< \gamma_{imp} > = 45.07\,^{\circ}$. The mean angle for Ganymede is $< \gamma_{imp} > = 45.41\,^{\circ}$ and shows the same shape. Note that an impact angle of $< \gamma_{imp} > = 0\,^{\circ}$ corresponds to a head-on collision, while $< \gamma_{imp} > = 90\,^{\circ}$ refers to a grazing impact.

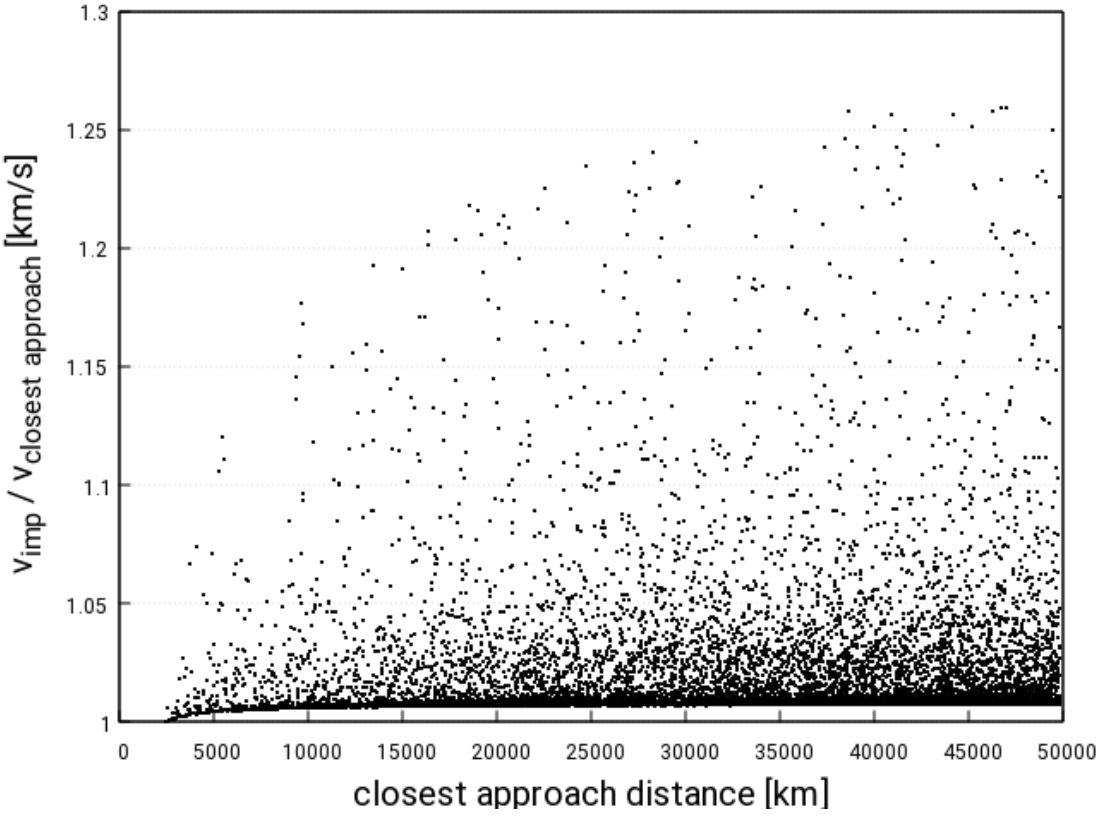

Figure 16: Comparison of impact velocities and the corresponding closest approach velocities depending on the closest approach distance. The intended systematic error to achieve high collision rates yields a maximum (mean) error of a factor of $\sigma = 1.259$ ($\sigma = 1.021$) in the time interval from entering the Hill sphere to colliding with Callisto.

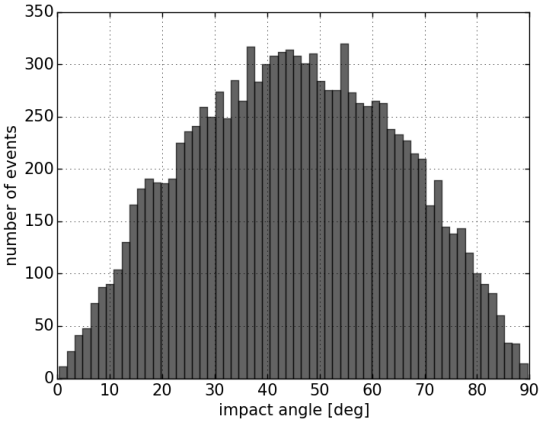

Figure 17: The impact angles for Callisto show a mostly symmetric, random distribution with a mean value of $< \gamma_{imp} > = 45.07\,^{\circ}$. $\gamma_{imp} = 0\,^{\circ}$ accounts for a head-on collision and $\gamma_{imp} = 90\,^{\circ}$ for a grazing impact.

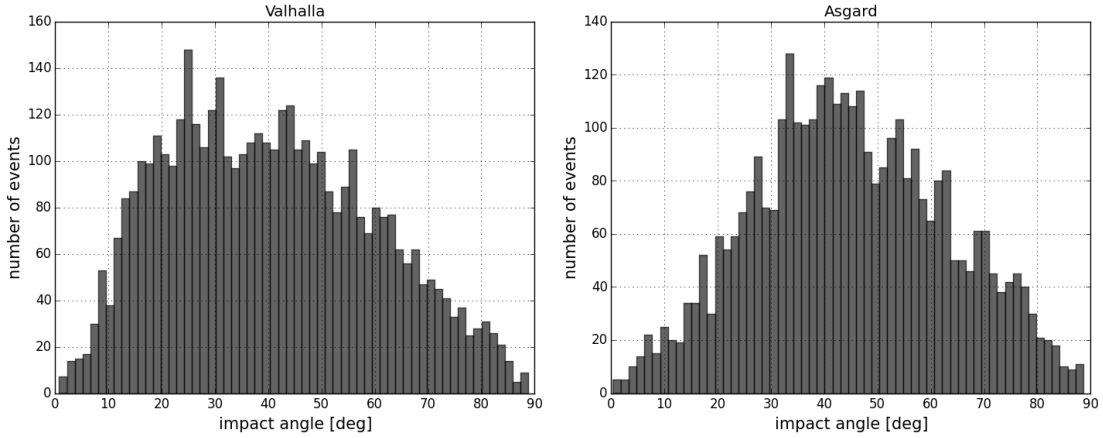

Figure 18: Impact angles for Valhalla-forming and Asgard-forming impacts. Since Valhalla has a relatively low latitude of $\phi = 14.7\,^{\circ}$, the mean impact angle is shifted towards the left. Asgard is located at a latitude of $\phi = 32.2\,^{\circ}$ and the shift appears to be smaller than the resolution of the data.

Figure 18 shows all collisions with latitudes of $4.7\,^{\circ} < \phi < 24.7\,^{\circ}$ for Valhalla-forming and $22.2^{\circ} < \phi < 42.2\,^{\circ}$ for Asgard-forming impacts. A clear shift to steeper impact angles appears for Valhalla-forming impacts. This result may be connected to the findings in section 2.3.2, where 'periapsis-particles' which are scattered into Jupiter's orbital plane, are more likely to collide with Callisto. This effect results in significantly lower impact

angles at low latitudes. The mean impact angles are $< \gamma_{imp} > = 40.34\,^{\circ}$ for Valhalla-forming impacts and $< \gamma_{imp} > = 44.92\,^{\circ}$ for Asgard-forming impacts. Even though a shift for Asgard can not be recognized in the plot, it should get visible at higher resolutions. In analogy to Table 5 we can further distinguish between prograde, retrograde, no periapsis and periapsis subsets for both craters, yielding slightly different results for the mean impact angles (see Table 6).

Table 7 shows the general result for the mean impact angles $< \gamma_{imp} >$ depending on the impact latitude ϕ_{imp}. Although all particles had random positions and velocities initially, they got scattered into Jupiter's orbital plane and seem to favour certain impact angles.

measurements	prograde	retrograde	no periapsis	periapsis
Valhalla	1,421	2,974	1,287	3,108
Asgard	1,240	2,331	1,081	1,290
$< \gamma_{imp} >$ [°]	prograde	retrograde	no periapsis	periapsis
Valhalla	41.6	39.73	39.23	40.8
Asgard	43.85	45.49	44.76	44.99

Table 6: Top: number of events for each subset. Since the latitude is limited to $\pm 10\,^{\circ}$ around the craters, the total number of measurements is lower than in Table 5. Bottom: Valhalla-forming impacts suggest that there may be a minor influence on the mean impact angle from each of the four attributes.

$\pm\phi_{imp}$ [°]	$< \gamma_{imp} >$ [°]
0-15	39.27
15-30	42.18
30-45	46.31
45-60	53.38
60-75	56.81
75-90	59.4

Table 7: The mean impact angles $< \gamma_{imp} >$ of certain latitude zones are shifted due to the influence of the Sun and Jupiter.

3 SPH simulations

In this section we present impact simulations on Callisto which are performed with the method of Smooth Particle Hydrodynamics (SPH). We also give brief summaries about both the used SPH code and the SPH method in general. From now on, we focus on the mass of the impactor rather than its velocity.

3.1 Introduction to SPH

Smooth Particle Hydrodynamics (SPH) is a numerical method to simulate the dynamical behaviour of macroscopic objects ranging from small Asteroids to Galaxy Clusters. The method was first described by Lucy (1977) and Gingold and Monaghan (1977) and is nowadays used for a broad range of astrophysical problems. First, SPH was only used in the *hydrodynamic* context (fluids), but it was later expanded to include elasto-plastic systems. The dynamical behaviour of a system is generally described by coupled, partial differential equations. Usually, these equations are not solvable and must be approximated by transforming them into a set of ordinary differential equations.

In contrast to grid-based methods, SPH uses a co-moving coordinate system. Such a system is also referred to as a *Lagrangian System*. A big advantage of this system is the fact that one is able to keep track of specific particles. Grid-based methods on the other hand have to include additional tracking algorithms to achieve similar effects. In astrophysics, SPH is mostly used to model three-dimensional problems like cosmic web formation, galaxy formation/evolution, star formation processes, gas dynamics (including magnetic fields) and solid-body collisions.

After Monaghan (1992), the basics of SPH can be described as follows: The system is split up into separate elements which are usually referred to as *SPH particles*. For the simulation setup, the particles are spread out across the simulation volume. Each particle has its own mass m_j, a density ρ_j and a position r_j. The momentum equation for an individual particle j is given by equation 19.

$$\frac{d^2 r_j}{dt^2} = -\frac{1}{\rho_j} \nabla P + F_j \tag{19}$$

∇P is the pressure gradient at a given position r_j and F_j is used for external forces such as gravity or electromagnetic fields which act on the particle. SPH-particles must not be mistaken for a real particles, they are rather numerical vehicles for tracking certain quantities (like density, pressure, etc.) in a given volume and therefore represent the values of the corresponding scalar or vector fields at specific positions r_j. A scalar quantity $f(r)$ in the 3D domain can be described by

$$f(r) = \int_V f(r')\delta(r - r')dr' \tag{20}$$

where δ denotes to the delta distribution and r' is an integration variable. The delta distribution can be replaced with the so-called *Kernel function* $W(r, h)$:

$$\lim_{h\to 0} W(r, h) = \delta(r) \tag{21}$$

For both the delta-function and the Kernel, the integration over the volume is equal to unity.

The quantity h is the so-called *smoothing length* which corresponds to the width of the Kernel and is usually derived from the SPH particle distribution of the system. The smoothing length describes how many neighbouring particles of a given particle j are included in the calculations for its quantities. If the distance from any particle i to particle j is larger than h, particle i has no influence (except gravitation) on particle j. Particles within h are weighted by the Kernel in such a way that very close particles contribute most to the change of particle j. The number of neighbouring particles typically ranges from 10 to 100. Too small numbers yield inaccurate calculations, whereas too large numbers are computationally demanding. The Kernel function can take different forms which corresponds to a different weighting of nearby particles. Some common forms are illustrated in Figure 19. The Kernel can easily be replaced in the code and can therefore be adapted to individual problems. Using any (symmetric) Kernel, we can transform equation 20 into the following form:

$$f(r) = \int_V f(r')W(r - r', h)dr' + O(h^2) \tag{22}$$

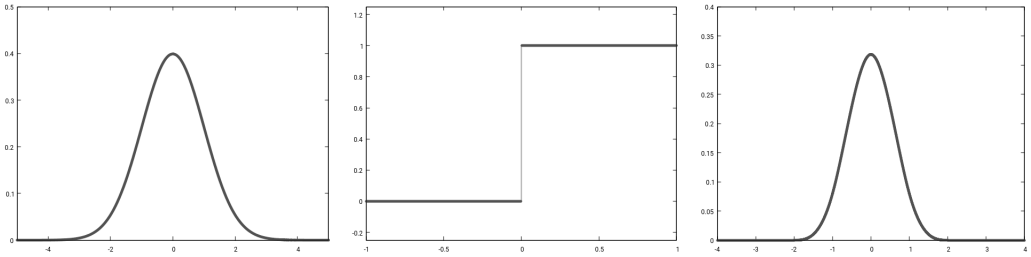

Figure 19: Different forms of the Kernel function $W(r, h)$. Left: Gaussian, Middle: Heaviside function, Right: cubic B-spline.

$O(h^2)$ refers to an error of the 2nd order, originating from the Kernel approximation. The integral is now expanded by $\rho(r')/\rho(r')$, where the mass of an SPH particle is given by $m(r') = \rho(r')dr'$. Since it is technically impossible to use an infinite number of SPH particles for a numerical computation, the integral transforms into a sum and yields equation 23,

$$f(r) \approx \sum_j \frac{m_j}{\rho_j} f(r_j) W(r - r_j, h) \tag{23}$$

where the summation includes all particles within the Kernel. $f(r)$ is now approximated by the SPH particles at the corresponding positions r. For example, the density of particle k is given by:

$$\rho(r_k) \approx \sum_j \frac{m_j}{\rho_j} \rho_j W(r_k - r_j, h) \tag{24}$$

$$\rho(r_k) \approx \sum_j m_j W(r_k - r_j, h) \tag{25}$$

One can also derive the gradient of equation 22. Since the gradient acts on r and not on r', it can be moved into the integral and thus only acts on the Kernel:

$$\nabla f(r) = \int_V f(r') \nabla W(r - r', h) dr' + O(h^2) \tag{26}$$

In analogy to equation 23, the gradient of a quantity $f(r)$ is therefore:

$$\nabla f(r) \approx \sum_j \frac{m_j}{\rho_j} f(r_j) \nabla W(r - r_j, h) \tag{27}$$

Interestingly, since the Kernel does not change and its gradient is therefore known analytically, one can easily derive the gradient of f from f itself.

3.2 The miluphCUDA code

For our simulations, we use the SPH code developed by Maindl et al. (2013) and Schäfer et al. (2016). It was specifically designed to model collisions between solid bodies (e.g. rocky planets, asteroids, etc.) and includes a damage model, brittle and porous materials, as well as self-gravity (Barnes-Hut tree with $n\ log(n)$ scaling). Time integration is done with an adaptive Runge-Kutta 3rd order scheme where the 3rd order solution is used as an error estimator. At the moment, one can either use the Murnaghan or Tillotson equations of state (EOS). Lately, the code was modified to support CUDA, the GPU computing interface developed by Nvidia, yielding an excellent performance in comparison to CPU-based parallelization methods (Schäfer et al., 2016). The miluphCUDA code uses a cubic B-spline Kernel as described in Monaghan and Lattanzio (1985) (see also Figure 19):

$$W(r,h) = \frac{s}{h^D} \begin{cases} 6(r/h)^3 - 6(r/h)^2 + 1 & \text{for } 0 \leq r/h \leq 1/2 \\ 2(1 - r/h)^3 & \text{for } 1/2 \leq r/h \leq 1 \\ 0 & \text{for } r/h > 1 \end{cases} \tag{28}$$

$$s = \begin{cases} \frac{4}{3} & \text{for 1D} \\ \frac{40}{7\pi} & \text{for 2D} \\ \frac{8}{\pi} & \text{for 3D} \end{cases} \tag{29}$$

r denotes to the distance between two interacting particles, h is the smoothing length and the factor s depends on the dimension of the system.

The code has been used successfully to simulate surface impacts, planetesimal and planetary embryo collisions, as well as surface sampling processes (Dvorak et al., 2015, 2017; Schäfer et al., 2017; Maindl, T. I. et al., 2015; Bancelin et al., 2017).

3.3 Object setup

3.3.1 Projectile: impact velocities, impact angles and properties

We select Callisto's largest crater – namely *Valhalla* – for further examination using the SPH code described above. From Table 3 we extract that the crater is located on the in-orbit-facing side of Callisto. This means that it is very likely that it was formed by a high-velocity, retrograde impact we discussed in section 2.3.2. Using the results of our n-body simulations, we define three plausible velocities for possible impact velocities:

- the maximum impact velocity of retrograde impacts with $v_{imp,1} = 19.89\,\mathrm{km/s}$
- the mean impact velocity of retrograde impacts with $v_{imp,2} = 18.23\,\mathrm{km/s}$
- the minimum impact velocity of retrograde impacts with $v_{imp,3} = 14.1\,\mathrm{km/s}$

Note that using only retrograde impact velocities implies that Callisto was already tidally locked when the basin was formed. Since this fact remains unknown, we define a fourth velocity dealing with a hypothetical low-velocity impact:

- the mean impact velocity of prograde impacts with $v_{imp,4} = 9.59\,\mathrm{km/s}$

Considering slightly different results for the impact angles at different latitudes (see Figure 18 and Table 7), we define three plausible angles for Valhalla:

- $\gamma_{imp,1} = 15\,^\circ$
- $\gamma_{imp,2} = 40\,^\circ$
- $\gamma_{imp,3} = 65\,^\circ$

An angle of $\gamma_{imp} = 90\,^\circ$ corresponds to a grazing impact, while $\gamma_{imp} = 0\,^\circ$ refers to a head-on impact. Note that the combination $v_{imp,2}$ and $\gamma_{imp,2}$ is the most plausible scenario. We use this combination as the standard setup for the projectile.

The projectile is completely made out of ice. Since the spatial resolution is larger than the projectile diameter, we use a refined spatial grid for the projectile to be able to accurately model its mass and diameter with approximately 80 SPH particles. *Projectile-particles* therefore also have a lower mass than *Callisto-particles*. However, we found that for our

aims it is not crucial to model the projectile accurately (see section 3.4.1) as long as the spatial resolution is of the same order of magnitude as the particle diameter.
We initially place the projectile directly onto Callistos surface to avoid additional acceleration by Callisto.
We perform several runs with different projectile masses to form craters with $D = 350\,\text{km}$, $D = 600\,\text{km}$ and $D = 980\,\text{km}$. We further introduce the ratio $\xi = d/D$ between the particle diameter and the crater diameter. The projectile mass and kinetic energy with given ξ and v_{imp} can be calculated easily:

$$m_{proj} = \frac{4\pi}{3}\rho_{proj}(0.5\xi D)^3 \tag{30}$$

$$E_{kin} = \frac{m_{proj}v_{imp}^2}{2} \tag{31}$$

3.3.2 Callisto: inner structure models

The inner structure of Callisto is not fully understood, which makes it difficult to define appropriate models. Considering Table 2, we define the following models with corresponding materials and layer thicknesses for our SPH runs:

- model 1 – core: iron (835 km), mantle: water (100 km), shell: ice (150 km)
- model 2 – core: basalt (1842 km), mantle: water (150 km), shell: ice (150 km)

We use the first model to reproduce craters with $D = 350\,\text{km}$ and the second model to reproduce craters with $D = 600\,\text{km}$ and $D = 980\,\text{km}$. Note that for the first model we use iron as core material instead of rock. This decision was made due to several reasons:

- The core is not substantially affected by relatively small impact events and we are only interested in surface effects.
- We are able to shrink Callisto by a factor of about 0.5 which results in an increase of spatial resolution by a factor of about 2.
- The error in curvature of the shrunken Callisto is negligible.
- The number of SPH particles needed for obtaining high resolutions (below 30 km in our case) decreases significantly.

The core sizes are adjusted so that the surface gravity of the models equals Callisto's surface gravity of $g = 1.236\,\mathrm{m\,s^{-2}}$. The total radii of the models are smaller than the real Callisto by factors of 0.45 (model 1) and 0.88 (model 2).

Since our main aim is the analysis of the projectile of the Valhalla-forming impact, we focus on the outermost layers – namely the icy shell and the water layer – at our simulations. Following Melosh (1989a) and the *Ring Tectonic Theory* (see section 1.4 for description), it is rather unimportant which material lies beneath a possible ocean (or a quasi-fluid asthenosphere in general), as long as it is denser than the asthenosphere itself.

The bright area of the Valhalla crater measures roughly 600 km to 800 km in diameter. It is unclear where the crater rim is located due to the fact that no classical crater rim can be seen. If we take the flat, innermost 350 km (in diameter) for the lower bound of the crater size, the transient crater depth will be approximately 70 km which is lower than the thickness of the ice shell. In this case, rings may not form in the outskirts of the crater. If we take the complete bright area for crater size, the transient crater will reach deep beneath the icy lithosphere, eventually producing many rings. Since we simulate the whole moon to avoid artificial effects, the spatial resolutions do not allow for analysing these rings.

The Lunar and Planetary Institute (`www.lpi.usra.edu/resources/cc/`) lists a rim diameter of $D = 980\,\mathrm{km}$ and an ejecta diameter of $D_{ejecta} = 1,800\,\mathrm{km}$ for Valhalla (Schenk and McKinnon, 1987; Schenk, 1991, 1993; McKinnon and Melosh, 1980) which differs significantly from the values $D = 350\,\mathrm{km}$ and $D_{ejecta} = 800\,\mathrm{km}$ obtained from Melosh (1989a). However, we use $D = 980\,\mathrm{km}$ as the upper bound of the crater diameter.

Although the inner structure models in Table 2 propose a relatively thick icy shell (of about 150 km), it seems to be inconsistent with the observed ring system of Valhalla. As mentioned in Melosh (1989a), the transient crater must be much deeper than the thickness of the shell to produce several rings in the outskirts of the crater. Since this is the case for Valhalla, a crater diameter significantly larger than $D = 350\,\mathrm{km}$ would be more consistent with observations. Another possibility may include significant thickening of the ice shell after the crater formation. Nevertheless, we analyze craters with $D = 350\,\mathrm{km}$ for evaluating the lower boundary of the projectile mass.

3.3.3 Simulation time, EOS, and resolutions

We estimate the simulation time with the timescale of the modification stage, using the maximum crater diameter of $D = 980\,\text{km}$:

$$t = \sqrt{D/g} \simeq 14.8\,\text{min} \tag{32}$$

A safety factor of 2 yields about 30 minutes simulation time. For the actual simulations, we use $t = 30\,\text{min}$ for $D = 350\,\text{km}$ and $t = 60\,\text{min}$ for $D = 600\,\text{km}$ and $D = 980\,\text{km}$, respectively to capture the whole crater formation process.

We use the Tillotson equation of state with the respective parameters given in Table 8.

material	ρ_0 [kg m^{-3}]	A [GPa]	B [GPa]	E_0 [MJ kg^{-1}]	E_{iv} [MJ kg^{-1}]	E_{cv} [MJ kg^{-1}]	a	b	α	β	μ [GPa]	Y_0 [GPa]
Basalt	2,700	26.7	26.7	487	4.72	18.2	0.5	1.5	5	5	22.7	3.5
Ice	917	9.47	9.47	10	0.773	3.04	0.3	0.1	10	5	2.8	1
Water	998	2.18	13.25	7	0.419	2.5	0.7	0.15	10	5	0	0

Table 8: Tillotson equations of state parameters, shear modulus μ and yield stress Y_0 (Benz and Asphaug, 1999; Brundage, 2013)

We can estimate the spatial resolution, which is given by the mean distance between two SPH particles, with a given particle number n by approximating Callisto with a cube and distributing the SPH particles homogeneously:

$$V_{Cal} = \frac{4\pi}{3} R_{Cal}^3 \tag{33}$$

$$mpd = \sqrt[3]{\frac{V_{Cal}}{n}} \tag{34}$$

The mean particle distance mpd corresponds to the *diameter* of a single SPH particle. The spatial resolution is given by the smoothing length $h = 2 \cdot mpd$. The cubic root of the particle number n is quite painful when one wants to achieve high spatial resolutions. We found that shrinking the object is much more effective than increasing the number of particles.

The typical size of the projectile should roughly be $1/10$ of the crater diameter (Melosh, 1989a). We prefer a numerical brute-force method to produce craters with adequate diameters via testing different projectile sizes. The technical limitations of the used GPU

(Nvidia GTX960, 4GB) only allow for particle numbers as high as $n = 450,000$. We use $n = 300,000$, yielding resolutions of about 52 km for model 1 and 102 km for model 2. The computation time for each run lasts about three hours.
We prefer a hexagonal arrangement of the initial SPH particle positions over a cubic one to avoid artificial, geometric effects. Both the time integration and the SPH method itself are 2nd order accurate methods.

3.4 Results and data analysis

This section summarizes our results of the impact simulations. Including test runs, we performed about 40 simulations in total.

3.4.1 Numerical effects of low-n projectiles

It is unclear whether a low number of SPH particles influences the crater formation process significantly. We therefore perform the exact same simulation with two different particle numbers for the projectile (see Figure 20). Both projectiles have the same mass ($m = 7 \cdot 10^{16}$ kg), impact velocity ($v_{imp} = 18.234$ km/s) and impact angle ($\gamma_{imp} = 40\,°$). The resulting craters are almost formed identically because the interactions between the particles take place within the smoothing length which is larger than the projectile itself. Therefore, the energy is transported similarly in both cases. This also implies that the size of the projectile is irrelevant, as long as it does not exceed the smoothing length. Moreover, one would assume that the single particle penetrates the surface more deeply than the 81 individual ones. This is not the case in our simulations. On the other hand, there are significantly more ejecta in the $n = 81$ run which origins from the relatively low-mass projectile particles in comparison to the single high-mass projectile particle.

3.4.2 Reconstruction of Valhalla

At the specific time of $t = 16.8 \pm 1.2$ min after the impact, the transient crater was found to be fully developed at all runs (for $D = 350$ km) and the material begins to rebound and flatten out the crater. During the modification phase, the crater disappears almost completely (see Figure 21). Interestingly, this flattening also takes place if no subsurface

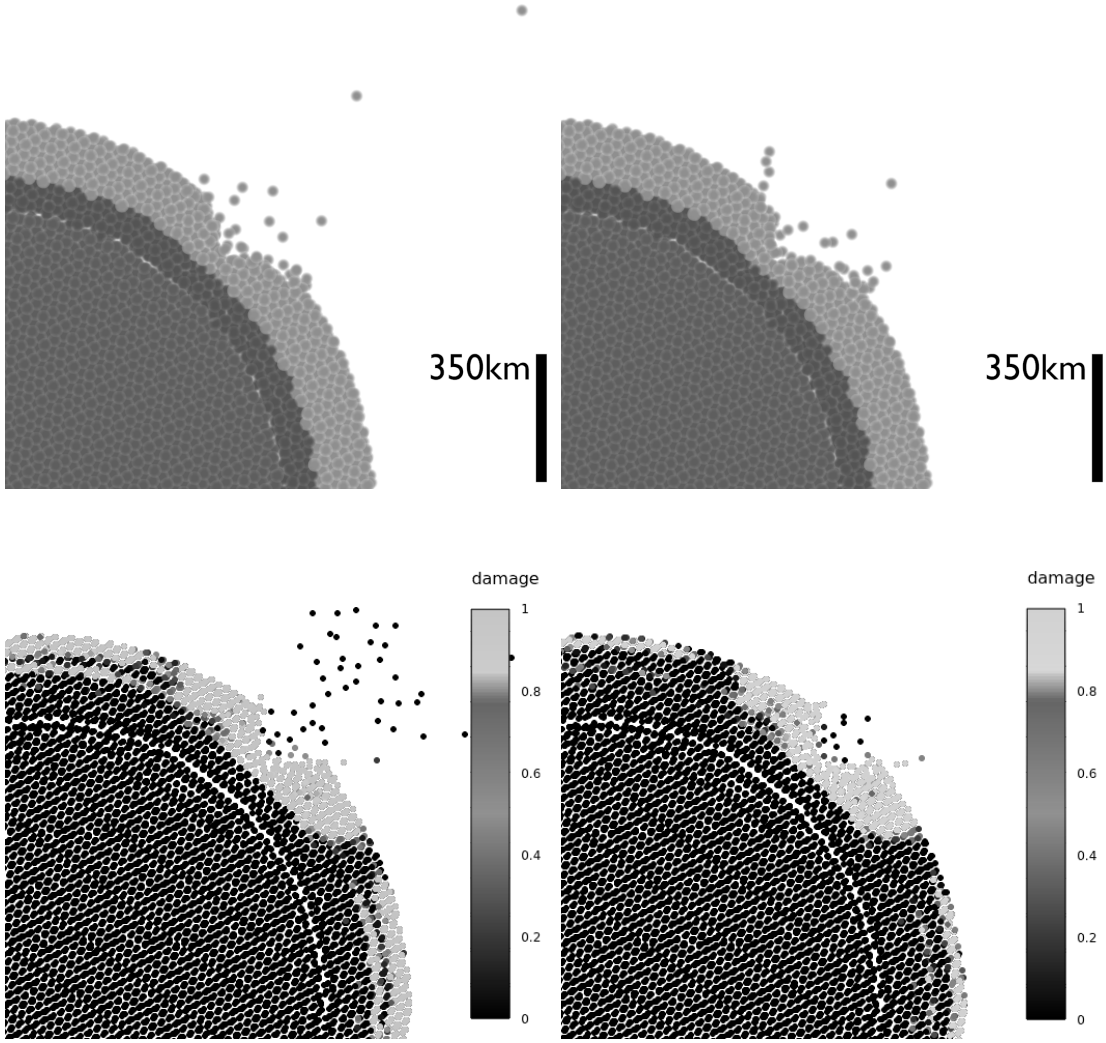

Figure 20: Snapshots of two simulations at $t = 16.8\,\text{min}$ (top row, materials) and $t = 6.6\,\text{min}$ (bottom row, damage). The first run (left column) uses a particle number of $n = 81$ while the second run (right column) uses a single particle for the projectile. The projectile is coming from the top at both simulations.

ocean is included in the simulations. The bottom panels in Figure 20 show the pattern of damaged material shortly after the impact. The results suggest that a non-damaged ring surrounds the crater, whereas the icy shell may break up due to large pressures from below. Since it is very difficult to obtain crater sizes quantitatively from the resulting

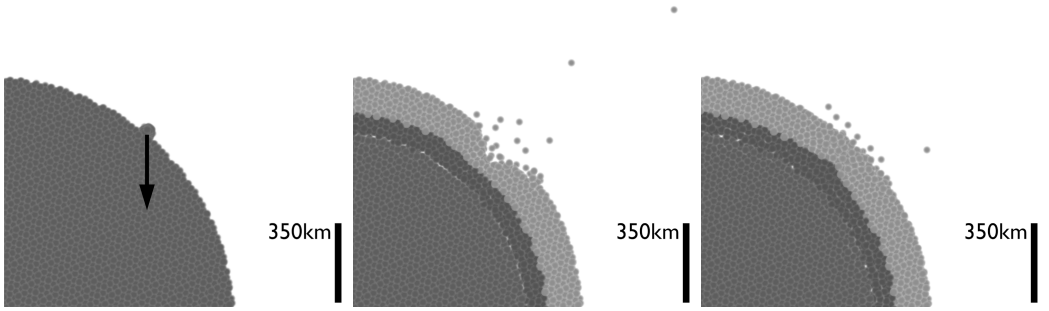

Figure 21: Time evolution of crater formation process. The first frame shows the projectile and its velocity vector shortly before the impact. The second frame shows the fully developed crater. In the last frame, the crater has almost completely disappeared due to the modification phase.

point clouds, we do a visual comparison using reference measures with lengths of 350 km, 600 km and 980 km respectively. Nevertheless, the accuracy of this technique is relatively imprecise and the measured crater sizes may vary up to $\epsilon_{350} = \pm 52\,\text{km}$, $\epsilon_{600} = \pm 102\,\text{km}$ and $\epsilon_{980} = {}^{+177}_{-273}\,\text{km}$. The errors ϵ_{980} originate from the minimum and maximum measured crater sizes rather than the spatial resolution.

The transient crater depths were found to be $H_{350} = 75 \pm 26\,\text{km}$, $H_{600} = 225 \pm 51\,\text{km}$ and $H_{980} = 300 \pm 51\,\text{km}$ for the respective crater diameters. It is more easy to measure crater depths because one can use the surface geometry of the moon as a reference plane as well as comparing the crater depths with the layer thicknesses. The errors for the crater depths are therefore approximately $\pm 0.5 \cdot h = \pm mpd$. In both the $D = 600\,\text{km}$ and $D = 980\,\text{km}$ runs the projectile penetrates the icy shell completely and reaches far into the asthenosphere (see Figure 22). We find that different impact angles produce similar transient crater diameters D, but significantly different transient crater depths H. Figure 23 shows three runs using the same projectile mass and velocity, but different impact angles. Since Valhalla has an extensive ring system which may had been produced by the

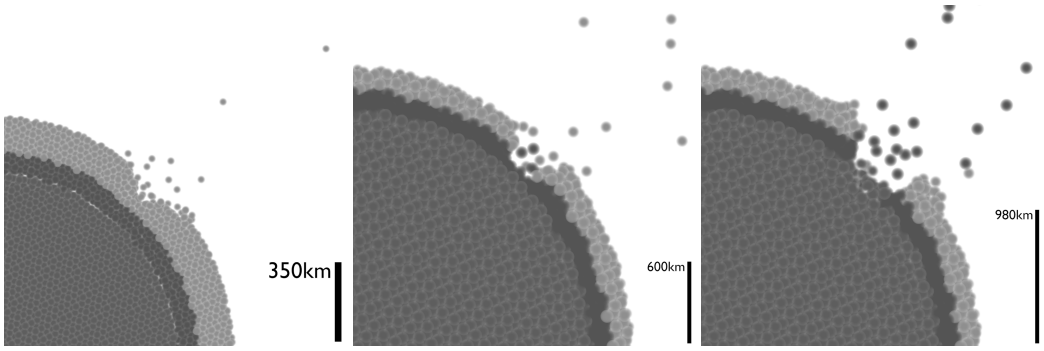

Figure 22: Transient crater depths rise with increasing transient crater diameter. Note that we use model 2 for the $D = 600\,\text{km}$ and $D = 980\,\text{km}$ runs.

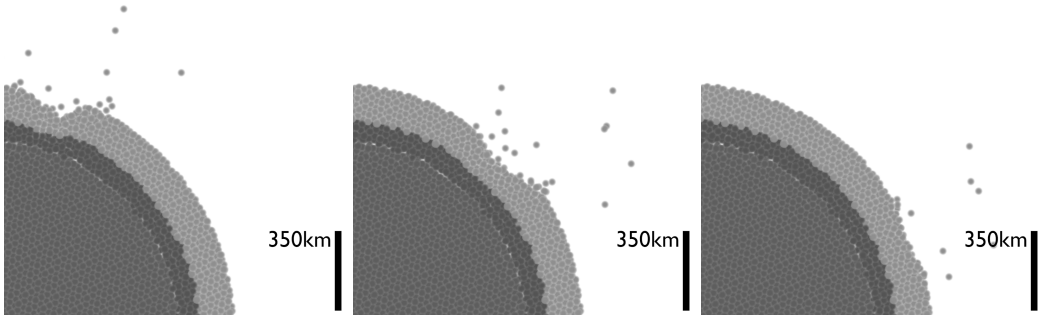

Figure 23: Steeper impact angles produce significantly deeper transient craters. The impact angles from left to right are $\gamma_{imp} = 15\,^\circ$, $\gamma_{imp} = 40\,^\circ$ and $\gamma_{imp} = 65\,^\circ$.

influence of a possible subsurface ocean (see section 1.4), we favour low impact angles over high ones. The projectile should be able to penetrate the icy shell and reach the asthenosphere.

Figure 24 summarizes our main results for each of the respective crater diameters. Non-

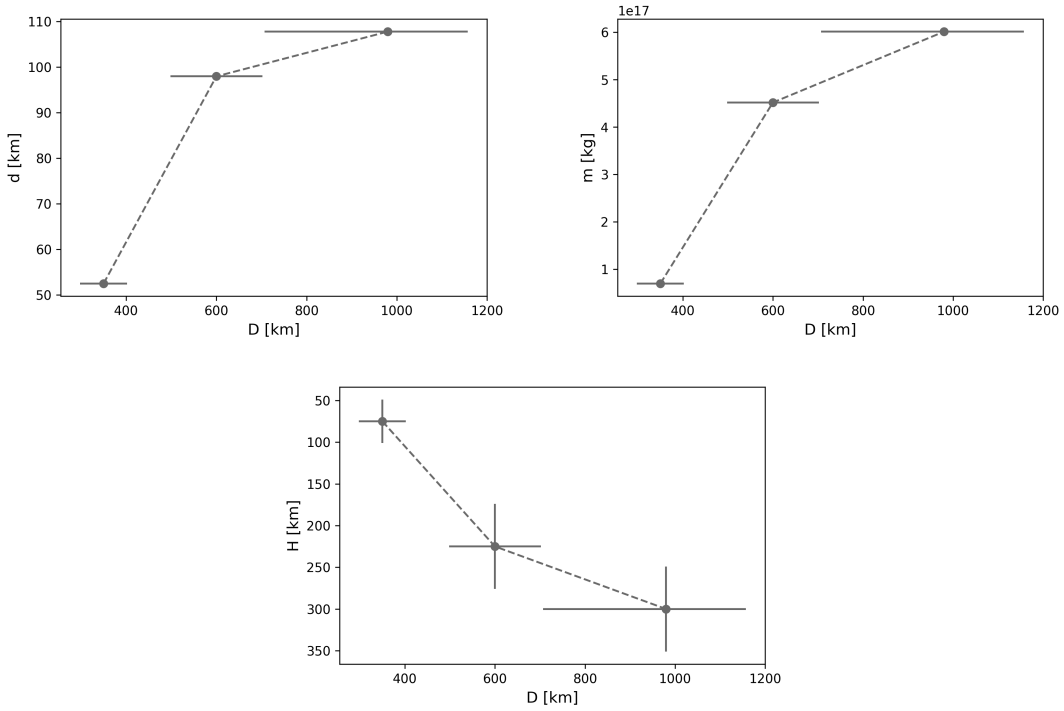

Figure 24: D and H are the measured transient crater diameters and depths. d and m are the used projectile diameters and masses.

linear trends can be seen for both the projectile properties and the transient crater depth-diameter ratios.

Until now we used an impact velocity of $v_{imp,2} = 18.234\,\mathrm{km/s}$. Using the kinetic energy of the projectile, we can estimate the corresponding projectile masses for the other three impact velocities. Table 9 summarizes these estimations. Figure 25 visualizes the mass estimations for the projectile depending on the impact velocity.

	$v_{imp,1}$	$v_{imp,2}$	$v_{imp,3}$	$v_{imp,4}$
r_{350} [km]	24.69	26.25	31.16	40.29
r_{600} [km]	47	49	58.16	75.2
r_{980} [km]	50.71	53.9	63.98	82.72
m_{350} [10^{16} kg]	5.78	6.95	11.62	25.11
m_{600} [10^{16} kg]	37.62	45.19	75.58	163.37
m_{980} [10^{16} kg]	50.08	60.15	100.6	217.45
ξ_{350} [1]	0.14	0.15	0.18	0.23
ξ_{600} [1]	0.15	0.16	0.19	0.25
ξ_{980} [1]	0.1	0.11	0.13	0.17

Table 9: Estimations of projectile properties obtained by simulation results using $v_{imp,2}$.

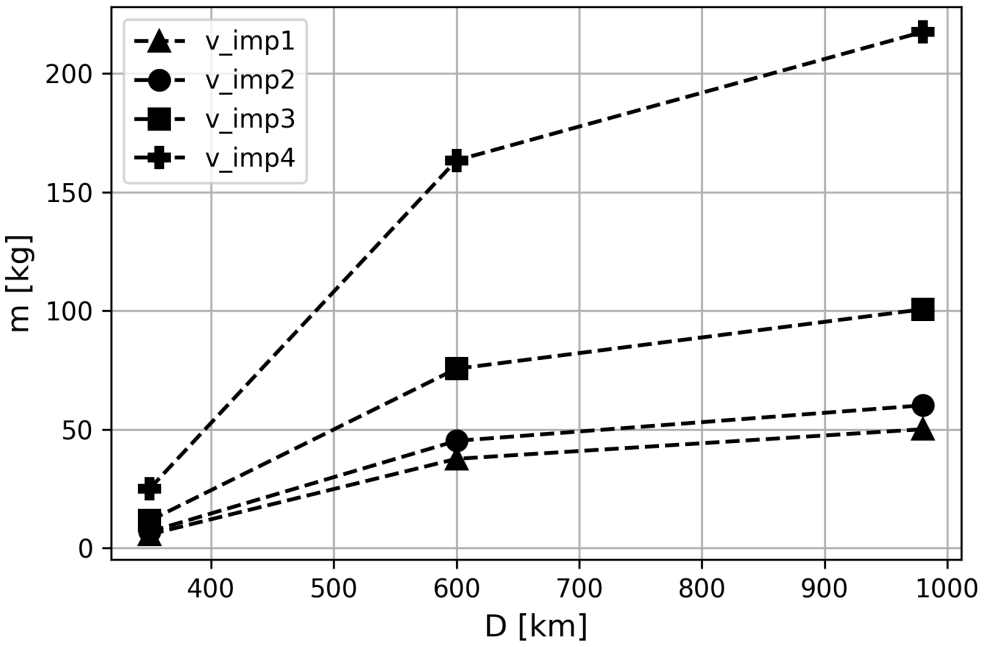

Figure 25: Mass estimates for different impact velocities. The graph for $v_{imp,2}$ is the same as in Figure 24. Note that the errorbars for D are not plotted in this figure.

The following considerations origin from our simulation results:

- If the transient crater is 350 km in diameter, a shell thickness of smaller than 150 km (Schenk, 2002) would be more consistent with Valhalla's ring system.
- If Callisto's shell has a thickness of about 150 km, high values for D appear to be more consistent with Valhalla's ring system.
- Considering the $D = 350\,\text{km}$ runs it seems that no liquid material is needed to flatten out the crater again during the modification stage. This implies that liquids are not necessarily responsible for filling the transient crater holes (see Figure 21).

4 Summary, conclusion and acknowledgements

4.1 Summary

The Jupiter system with its four Galilean moons was visited by several probes which gave deep insights into this foreign world. Callisto, the outermost of the four moons, was discovered 1610 together with its three companions Io, Europa and Ganymede. In this thesis, we aim to analyse Callisto's biggest impact crater – the Valhalla basin.

Pioneer 10 and 11 delivered the first high-resolution images of Callisto's heavily cratered surface. This implied a very old and inactive body, originating from the earliest phases of Solar system formation. Later, Voyager 1 and 2 observed Callisto with even higher resolution, receiving details of her icy surface and big crater systems like Valhalla and Asgard. In 1989, Galileo set out for Callisto, obtaining deep insights about surface compositions, crater morphologies, magnetic fields and the inner structure. In analogy to Europa and Ganymede, Galileos measurements implied a subsurface ocean on Callisto.

Callisto's period around Jupiter is $P = 16.69$ days and her semi-major axis is $a = 1,882,700$ km. She stays in a 7:3 MMR with Ganymede and has a bound rotation with Jupiter. Her radius is $R = 2,410.3$ km which makes her as big as Mercury. The density of $\rho = 1,834.4\,\mathrm{kg\,m^{-3}}$ implies a rocky/icy inner structure.

The Valhalla crater system measures approximately 3,000 kilometers in diameter, containing a bright central area of about 700 kilometers, a ridge system as well as a ring system in the outskirts of the crater. The crater formation process itself is very complex and many details are still poorly understood. In this thesis, we reconstruct the Valhalla crater formation using both n-body and SPH simulations to obtain the impact geometry and the properties of the impactor.

For the n-body simulations, we use the Sun, Jupiter, Ganymede and Callisto as massive bodies and measure collisions of randomly initialized test particles with Ganymede and Callisto. We use two operating modes, the normal mode and the moon mode, to gain a high collision rate. Although this approach causes a systematic error (see Figure 16), it was found to yield plausible results for typical impact velocities and impact angles.

We use a RKCK integrator with embedded adaptive stepsize to integrate the system over a period of 1.4 years (normal mode) and 130 minutes (moon mode). The relative error

tolerance was set to $\epsilon = 10^{-11}$ which yielded a global error of 121.5 km in space and 0.009 m/s in velocity.

The initial conditions for the test particles at the edge of Jupiter's Hill sphere are estimated with several constrains on the orbit of the particles. We find typical, maximum, relative velocities to Jupiter to be $v_{rel,orbital} = 670\,\mathrm{m/s}$, $v_{rel,radial} = 65\,\mathrm{m/s}$ and $v_{rel,vertical} = 4,534\,\mathrm{m/s}$.

Our main results are summarized in Figure 15. The collision analysis for the moons significantly favours retrograde impacts and particles which already had their closest approach to Jupiter. The high number of measurements allow for defining four plausible impact velocities ($v_{imp,1} = 19.89\,\mathrm{km/s}$, $v_{imp,2} = 18.23\,\mathrm{km/s}$, $v_{imp,3} = 14.1\,\mathrm{km/s}$, $v_{imp,4} = 9.59\,\mathrm{km/s}$) and three impact angles ($\gamma_{imp,1} = 15\,^\circ$, $\gamma_{imp,2} = 40\,^\circ$, $\gamma_{imp,2} = 65\,^\circ$) for Callisto's Valhalla crater. Apparently, there is a correlation between the impact angle and the latitude of the crater, favouring slightly steeper impact angles.

We use the newly attained knowledge of typical impact velocities and impact angles to perform actual impact simulations with a Smooth Particle Hydrodynamics (SPH) method. The miluphCUDA code, developed by Maindl et al. (2013) and Schäfer et al. (2016), was designed to accurately model collision events of solid bodies and uses the CUDA GPU-computing interface by Nvidia.

We use a simple model for the projectile, consisting of about 80 SPH particles made out of ice. The standard setup for the impact geometry is the combination $v_{imp,2}$ and $\gamma_{imp,2}$. We define two different models for Callisto with one including an iron core and the other one including a rocky core. We aim to reproduce the Valhalla basin which may have a diameter between 350 km and 980 km.

We use the Tillotson equations of state and our spatial resolutions are 52 km and 102 km, depending on the used model for Callisto. The simulation times range between 30 minutes and one hour.

Our results show that the projectile can be modelled by a single SPH particle without producing unwanted numerical effects, as long as its diameter does not exceed the smoothing length. The crater formation of the Valhalla basin turns out to be highly complex. During the modification phase, the transient crater is flattened out completely, even without a subsurface ocean. We measure transient crater diameters and depths which are summarized in

Figure 24. We find that the impact angle has a significant influence on the transient crater depth, whereas the transient crater diameter is not affected. Using the simulation results, we are able to estimate projectile properties depending on plausible impact velocities (see Table 9 and Figure 25).

4.2 Zusammenfassung

Das Jupiter-System mit seinen zahlreichen Monden wurde bereits durch diverse Sondenmissionen untersucht, welche tiefe Einblicke in diese fremde Welt lieferten. Kallisto, der äußerste der vier Galileischen Monde, wurde 1610 gemeinsam mit den anderen dreien Io, Europa und Ganymed entdeckt. In dieser Arbeit untersuchen wir den größten Impakt Krater auf Kallisto – den Valhalla Krater.

Pioneer 10 und 11 lieferten die ersten hochauflösenden Bilder der stark verkrateren Oberfläche. Dies führte zu der Annahme, dass Kallisto keine aktive Geologie aufweist und dass die Oberfläche seit den Frühphasen des Sonnensystems nahezu unverändert ist. Später erforschten Voyager 1 und 2 Kallisto mit verbesserter Technik und enthüllten noch mehr Details ihrer vereisten Kruste und der großen Impaktkrater wie Valhalla und Asgard. 1989 startete die Sonde Galileo und lieferte neue Erkenntnisse über Kallisto's chemische Oberflächenzusammensetzung, Kratermorphologien, Magnetfelder sowie den inneren Aufbau. In Analogie zu Europa und Ganymed vermutet man durch die Messungen von Galileo ebenso auf Kallisto einen unterirdischer Ozean aus flüssigem Wasser.

Kallisto hat eine Umlaufperiode von $P = 16.69$ Tagen und ihre große Halbachse beträgt $a = 1,882,700$ km. Sie steht in einer 7:3 Bahnresonanz mit Ganymed und hat eine gebundene Rotation um Jupiter. Kallistos Radius beträgt $R = 2,410.3$ km, was sie gleich groß wie Merkur macht. Eine Dichte von $\rho = 1,834.4\,\mathrm{kg\,m^{-3}}$ impliziert eine Mischung aus Gestein und Eis für ihren inneren Aufbau.

Das Valhalla Krater System misst in etwa 3,000 Kilometer im Durchmesser. Es besteht aus einem hellen, zentralen Gebiet mit etwa 700 Kilometer im Durchmesser, einem konzentrischen Gebirgskamm und einem Ring-System in den äußeren Bereichen. Der Entstehungsprozess des Kraters ist sehr komplex und viele Details sind bis heute unklar. In dieser Arbeit rekonstruieren wir den Entstehungsprozess des Valhalla-Kraters mit Hilfe von n-body und SPH Simulationen, um vor allem die Impaktgeometrie und die Eigen-

schaften des Impaktors zu bestimmen.

Für die n-body Simulationen verwenden wir die Sonne, Jupiter, Ganymed und Kallisto als massebehaftete Körper und messen Kollisionen zwischen den Monden und Testteilchen, welche mit zufälligen Anfangsbedingungen initialisiert werden. Der Code verwendet zwei unterschiedliche Modi, den normal mode und den moon mode, um eine hohe Kollisionsrate zu erhalten. Obwohl dieses Vorgehen einen systematischen Fehler verursacht (siehe Abbildung 16), zeigen die Ergebnisse plausible Werte für typische Impaktgeschwindigkeiten und Impaktwinkel.

Wir verwenden einen RKCK Integrator mit eingebauter adaptiver Schrittweite, um das System über einen Zeitraum von 1.4 Jahren (normal mode) und 130 Minuten (moon mode) zu entwickeln. Die relative Fehlertoleranz beträgt $\epsilon = 10^{-11}$, was einen globalen Fehler von 121.5 km im Raume und 0.009 m/s in der Geschwindigkeit verursacht.

Die Anfangsbedingungen für die Testteilchen, welche am Rand von Jupiters Hill-Sphäre initialisiert werden, werden durch einige Einschränkungen bezüglich der möglichen Orbits abgeschätzt. Wir finden typische, maximale, Relativgeschwindigkeiten von $v_{rel,orbital} = 670\,\mathrm{m/s}$, $v_{rel,radial} = 65\,\mathrm{m/s}$ und $v_{rel,vertical} = 4,534\,\mathrm{m/s}$ zu Jupiter.

Unsere Resultate sind in Abbildung 15 zusammengefasst. Die Kollisionsanalyse bevorzugt retrograde Impakte mit Testteilchen, welche bereits zuvor ihre größte Annäherung an Jupiter vollzogen hatten. Die hohe Anzahl an gemessenen Kollisionen erlaubt es uns typische Impaktgeschwindigkeiten ($v_{imp,1} = 19.89\,\mathrm{km/s}$, $v_{imp,2} = 18.23\,\mathrm{km/s}$, $v_{imp,3} = 14.1\,\mathrm{km/s}$, $v_{imp,4} = 9.59\,\mathrm{km/s}$) und typische Impaktwinkel ($\gamma_{imp,1} = 15\,^\circ$, $\gamma_{imp,2} = 40\,^\circ$, $\gamma_{imp,2} = 65\,^\circ$) für den Valhalla-Krater zu definieren. Es existiert einen Zusammenhang zwischen dem Impaktwinkel und der geografischen Breite des Kraters, welche etwas steilere Impaktwinkel bevorzugt.

Wir verwenden unser neu gewonnenes Wissen über typische Impaktgeschwindigkeiten und Impaktwinkel, um den eigentlichen Impakt mit Hilfe einer SPH Methode zu simulieren. Der miluphCUDA Code, welcher von Maindl et al. (2013) and Schäfer et al. (2016) entwickelt wurde, wurde speziell für Festkörperkollisionen designed. Er verwendet das CUDA GPU-computing Interface von Nvidia.

Wir verwenden ein einfaches Modell für das Projektil, welches aus ca. 80 SPH Teilchen aus Eis aufgebaut ist. Die Kombination von $v_{imp,2}$ und $\gamma_{imp,2}$ stellt das Standardsetup für

die Impaktgeometrie dar. Wir definieren zwei verschiedene Modelle für Kallisto. Das erste Modell beinhaltet einen Eisenkern, das zweite einen Gesteinskern. Wir reproduzieren den Valhalla Krater, welcher wahrscheinlich einen Durchmesser zwischen 350 km und 980 km hat.
Wir verwenden die Tillotson Zustandsgleichung und unsere räumlichen Auflösungen betragen 52 km und 102 km, abhängig von dem verwendeten Modell von Kallisto. Die Simulationszeiten betragen zwischen 30 Minuten und einer Stunde.
Unsere Resultate zeigen, dass das Projektil aus einem einzigen SPH-Teilchen bestehen kann, ohne ungewollte numerische Effekte zu erzeugen. Der Projektildurchmesser darf dabei jedoch die Glättungslänge nicht überschreiten. Der Entstehungsprozess des Valhalla-Kraters ist extrem komplex. Während der Modifikationsphase wird der transiente Krater wieder komplett geglättet. Dieser Prozess passiert sogar ohne einen unterirdischen Ozean. Wir messen transiente Kraterdurchmesser und Kratertiefen, welche in Abbildung 24 zusammengefasst sind. Wir stellen fest, dass der Impaktwinkel signifikante Auswirkungen auf die Kratertiefe hat, der Kraterdurchmesser jedoch unbeeinflusst bleibt. Durch die Verwendung der Simulationsresultate können wir die Eigenschaften des Projektils abschätzen. Diese sind abhängig von den verwendeten Impaktgeschwindigkeiten (siehe Tabelle 9 und Abbildung 25).

4.3 Conclusion

Callisto's Valhalla basin is an extraordinary feature in the whole range of complex craters. Since there is no classical crater rim, it is difficult to constrain plausible crater sizes. The extensive ring system in the outskirts of the crater may play a major role for determining the properties of the icy shell and a possible subsurface ocean.
During the work on this thesis I noticed that a lot of science can be extracted from this topic with relatively low efforts. This fact makes Callisto an interesting object to study and to think about. Future work may be more sophisticated in terms of covering the full parameter space in n-body simulations and higher spatial resolutions in SPH simulations. At a certain point we may be able to resolve the details of the crater formation process of Valhalla which may give completely new insights into Callisto's inner structure. Studying other large multi-ring basins on Callisto may reveal geometric information about the

interior in the respective regions.

We experienced challenges with choosing accurate initial conditions for the n-body simulations which may result in non-accurate estimations for the projectile properties. The impact velocities may be higher due to highly inclined and highly eccentric initial orbits of the projectile. We currently investigate this topic with more sophisticated algorithms (Winter et al. (2017) in prep. EPSC 2017).

We also ran into challenges with the spatial resolution for the SPH runs, which forced us to trim the used models of Callisto in order to get realistic results. However, with higher computational power we may be able to reach high spatial resolutions in the near future.

4.4 Acknowledgements

I want to thank Thomas Maindl for the huge amount of useful comments, discussions and his tremendous helpfulness which allowed me to write this thesis. I learned many essential skills for doing complex scientific simulations, as well as an overall understanding of collision events in the context of planetary systems. I would have been lost using the miluphCUDA code without the help of Thomas Maindl. Also Christoph Burger contributed many valuable comments about the details of the used simulation techniques. Many thanks to Rudolf Dvorak, who supervised this thesis and who supported me in the overall process of attaining the MSc degree. I am thankful for his help at any type of problems which occurred during the process of writing. Many thanks to Christoph Schäfer, who supported me with solving technical problems concerning the SPH simulations. I want to acknowledge Max Zimmermann, Jan Florian, Nikolaus Sulzenauer, Ernst Dorfi, Christina Petschnigg, Markus Ambrosch, Nina Némec, João Alves, Max Wladar, Ákos Bazsó, Markus Obernosterer, Sara Wanek, Stefan Brandner and Andreas Karnthaler for enlightening comments about specific aspects of this thesis. Finally I would like to thank my parents for their continuous psychological and financial support, allowing me to write this thesis.

5 Appendix

Callisto	a	b	t [yr]	v_{imp} [km/s]	γ_{imp}[°]	z [km]	h_{imp} [s]
	1	1	0.893	18.455	48.872	-1730	8
	1	1	1.031	15.899	43.421	1404	9
	0	1	1.054	8.173	39.509	-1561	12
	1	1	1.191	19.320	47.288	-860	7
	0	1	1.050	5.268	82.872	-1785	15
	1	1	1.172	19.660	56.202	-2020	7
	1	1	1.076	17.145	4.738	-1305	7
	0	1	0.922	11.537	49.294	-336	17
	0	0	0.753	11.372	41.143	-635	10
	1	1	1.146	19.487	60.987	2130	7
	0	1	1.076	7.476	54.622	-549	15
	1	1	1.031	18.935	23.646	-569	7
	0	0	1.231	4.074	57.087	-1922	20
	1	1	1.099	19.241	48.379	-225	7
	0	0	0.777	10.814	36.593	-820	10
	0	0	0.940	8.836	79.320	1159	13
	0	0	0.960	12.285	11.536	1402	9
	0	0	1.110	4.879	73.010	-1072	14
	0	1	0.823	10.065	79.211	1003	12
	1	0	1.044	19.218	38.745	496	8
	1	1	0.825	18.193	16.970	485	7
	1	1	1.127	19.683	47.934	-549	7
	0	1	0.938	12.623	42.366	-2390	9
	1	1	1.105	19.676	30.158	322	7

Table 10: Collisions for Callisto in normal mode. a: front (0) or back (1) impact, b: Jupiter periapsis no (0) or yes (1), t: simulation time, v_{imp}: impact velocity, γ_{imp}: impact angle, z: height above equator, h_{imp}: stepsize at impact

Ganymede	a	b	t [yr]	v_{imp} [km/s]	γ_{imp}[°]	z [km]	h_{imp} [s]
	0	1	0.747	17.227	66.064	-300	9
	0	0	0.969	7.951	26.121	1438	11
	0	1	0.996	10.960	56.249	-1050	11
	1	1	1.231	25.976	14.868	-782	6
	1	1	0.694	22.894	19.312	618	6
	1	1	1.307	25.077	30.234	-663	7
	1	1	1.309	25.964	7.712	142	5
	0	0	0.944	15.801	45.622	1945	10
	1	0	1.117	25.968	52.420	-1482	7
	0	0	1.027	9.222	23.599	181	9
	1	1	0.810	22.097	61.962	-2495	7
	0	1	0.985	11.752	72.605	2220	13
	1	0	1.219	22.534	54.441	-414	7
	1	1	1.386	25.507	54.499	1559	6
	1	1	0.969	26.095	38.883	521	6
	1	0	1.198	23.933	22.110	-917	6
	1	0	1.268	22.543	44.415	-1673	7
	1	0	0.758	25.265	67.680	-1623	6
	0	1	0.629	17.096	32.395	-899	8
	0	1	0.975	10.194	59.406	-92	12
	1	0	0.819	22.647	29.664	-799	7
	1	0	0.810	23.591	25.333	769	6
	0	0	0.736	17.802	22.561	-1552	8
	1	1	1.202	25.461	47.031	604	7
	0	0	0.652	14.969	79.291	-1474	9
	1	1	1.182	26.086	16.420	701	6
	1	0	0.882	26.204	19.011	-649	6
	0	1	0.922	18.704	13.084	1041	7
	1	0	0.867	23.498	42.322	851	7
	1	1	0.828	23.364	54.356	1734	7
	1	0	0.835	25.864	51.235	-268	6
	1	0	0.803	20.536	18.111	-725	7
	1	1	0.789	23.257	53.694	332	7
	0	0	1.006	11.844	44.044	1913	9
	1	1	1.065	24.705	31.399	1225	6
	1	1	0.930	26.183	45.036	-652	6
	1	1	0.850	25.716	44.014	-1748	6
	0	1	0.976	12.730	20.650	-877	9
	1	0	1.000	26.157	64.819	1869	7

Table 11: Collisions for Ganymede in normal mode. a: front (0) or back (1) impact, b: Jupiter periapsis no (0) or yes (1), t: simulation time, v_{imp}: impact velocity, γ_{imp}: impact angle, z: height above equator, h_{imp}: stepsize at impact

References

J. D. Anderson, E. L. Lau, W. L. Sjogren, G. Schubert, and W. B. Moore. Gravitational evidence for an undifferentiated Callisto. *Nature*, 387:264–266, May 1997. doi: 10.1038/387264a0.

J. D. Anderson, G. Schubert, R. A. Jacobson, E. L. Lau, W. B. Moore, and W. L. Sjo Gren. Distribution of Rock, Metals, and Ices in Callisto. *Science*, 280:1573, June 1998. doi: 10.1126/science.280.5369.1573.

J. D. Anderson, R. A. Jacobson, T. P. McElrath, W. B. Moore, G. Schubert, and P. C. Thomas. Shape, mean radius, gravity field, and interior structure of callisto. *Icarus*, 153:157–161, September 2001. doi: 10.1006/icar.2001.6664.

R. B. Baldwin. The tsunami model of the origin of ring structures concentric with large lunar craters. *Physics of the Earth and Planetary Interiors*, 6:327–339, 1972. doi: 10.1016/0031-9201(72)90056-8.

D. Bancelin, E. Pilat-Lohinger, T. I. Maindl, F. Ragossnig, and C. Schäfer. The Influence of Orbital Resonances on the Water Transport to Objects in the Circumprimary Habitable Zone of Binary Star Systems. *AJ*, 153:269, June 2017. doi: 10.3847/1538-3881/aa7202.

K. C. Bender, R. Greeley, J. W. Rice, Jr., and D. E. Wilhelms. Geologic Map of Callisto. In *Lunar and Planetary Science Conference*, volume 25 of *Lunar and Planetary Science Conference*, page 91, March 1994.

K. C. Bender, K. S. Homan, R. Greeley, C. R. Chapman, J. Moore, C. Pilcher, W. J. Merline, J. W. Head, M. Belton, T. V. Johnson, and SSI Team. The Asgard and Valhalla regions - Galileo's new views of Callisto. In *Lunar and Planetary Science Conference*, volume 28 of *Lunar and Planetary Inst. Technical Report*, page .89, March 1997.

W. Benz and E. Asphaug. Catastrophic Disruptions Revisited. *Icarus*, 142:5–20, November 1999. doi: 10.1006/icar.1999.6204.

Aaron L. Brundage. Implementation of Tillotson Equation of State for Hypervelocity Impact of Metals, Geologic Materials, and Liquids. *Procedia Engineering*, 58:461-470, June 2013.

R. W. Carlson. A Tenuous Carbon Dioxide Atmosphere on Jupiter's Moon Callisto. *Science*, 283:820, February 1999. doi: 10.1126/science.283.5403.820.

R. W. Carlson, J. C. Bhattacharyya, B. A. Smith, T. V. Johnson, B. Hidayat, S. A. Smith, G. E. Taylor, B. O'Leary, and R. T. Brinkmann. An Atmosphere on Ganymede from Its Occultation of SAO 186800 on 7 June 1972. *Science*, 182:53–55, October 1973. doi: 10.1126/science.182.4107.53.

J. R. Cash and Alan H. Karp. A variable order runge-kutta method for initial value problems with rapidly varying right-hand sides. *ACM Trans. Math. Softw.*, 16(3): 201–222, September 1990. ISSN 0098-3500. doi: 10.1145/79505.79507. URL `http://doi.acm.org/10.1145/79505.79507`. (last accessed: 15 Nov 2016).

S. K. Croft. Cratering on Ganymede and Callisto: Comparisons with the Terrestrial Planets. In *Lunar and Planetary Science Conference*, volume 12 of *Lunar and Planetary Science Conference*, pages 187–189, March 1981.

R. Dvorak, T. I. Maindl, C. Burger, C. Schäfer, and R. Speith. Planetary Systems and the Formation of Habitable Planets. *Nonlinear Phenomena in Complex Systems, Vol.18, No.3, pp. 310-325*, 18:310–325, September 2015.

R. Dvorak, B. Loibnegger, and T. I. Maindl. Possible origin of Theia, the Moon-forming impactor with Earth. *Astronomische Nachrichten*, 338:366–374, May 2017. doi: 10.1002/asna.201613209.

G. K. Gilbert. *The Moon's face: a study of the origin of its features*. Bulletin of the Philosophical Society of Washington, April 1893. URL `https://babel.hathitrust.org/cgi/pt?id=hvd.32044080587637;view=1up;seq=5`. (last accessed: 11 Jan 2017).

R. A. Gingold and J. J. Monaghan. Smoothed particle hydrodynamics - Theory and

application to non-spherical stars. *MNRAS*, 181:375–389, November 1977. doi: 10.1093/mnras/181.3.375.

W. K. Hartmann and F. G. Yale. Lunar Crater Counts. IV: Mare Orientale and Its Basin System. *Communications of the Lunar and Planetary Laboratory*, 7:131–138, 1968.

J. W. Head. Origin of outer rings in lunar multi-ringed basins - Evidence from morphology and ring spacing. In D. J. Roddy, R. O. Pepin, and R. B. Merrill, editors, *Impact and Explosion Cratering: Planetary and Terrestrial Implications*, pages 563–573, 1977.

P. Helfenstein, J. Veverka, and J. Hillier. Callisto's Regolith: A Better Estimate of the Ice/Silicate Ratio. In *Lunar and Planetary Science Conference*, volume 26 of *Lunar and Planetary Science Conference*, March 1995.

C. A. Hodges and D. E. Wilhelms. Formation of lunar basin rings. *Icarus*, 34:294–323, May 1978. doi: 10.1016/0019-1035(78)90169-0.

R. A. Jacobson and M. Brozovic. Natural satellite ephemerides at jpl. *IAU General Assembly*, 22:2233438, August 2015.

NASA JPL. Voyager 2 callisto, July 1979. URL `http://www.ciclops.org/view/3603/Callisto-False-Color`. (last accessed: 21 Jan 2017).

K. K. Khurana, M. G. Kivelson, D. J. Stevenson, G. Schubert, C. T. Russell, R. J. Walker, and C. Polanskey. Induced magnetic fields as evidence for subsurface oceans in Europa and Callisto. *Nature*, 395:777–780, October 1998. doi: 10.1038/27394.

M. G. Kivelson, K. K. Khurana, D. J. Stevenson, L. Bennett, S. Joy, C. T. Russell, R. J. Walker, C. Zimmer, and C. Polanskey. Europa and Callisto: Induced or intrinsic fields in a periodically varying plasma environment. *JGR*, 104:4609–4626, March 1999. doi: 10.1029/1998JA900095.

O. L. Kuskov and V. A. Kronrod. Models of the Internal Structure of Callisto. *Solar System Research*, 39:283–301, July 2005. doi: 10.1007/s11208-005-0043-0.

L. B. Lucy. A numerical approach to the testing of the fission hypothesis. *AJ*, 82:1013–1024, December 1977. doi: 10.1086/112164.

T. I. Maindl, C. Schäfer, R. Speith, Á. Süli, E. Forgács-Dajka, and R. Dvorak. SPH-based simulation of multi-material asteroid collisions. *Astronomische Nachrichten*, 334:996, November 2013. doi: 10.1002/asna.201311979.

Maindl, T. I., Dvorak, R., Lammer, H., Güdel, M., Schäfer, C., Speith, R., Odert, P., Erkaev, N. V., Kislyakova, K. G., and Pilat-Lohinger, E. Impact induced surface heating by planetesimals on early mars. *A&A*, 574:A22, 2015. doi: 10.1051/0004-6361/201424256. URL `https://doi.org/10.1051/0004-6361/201424256`.

W. B. McKinnon and H. J. Melosh. Evolution of planetary lithospheres - Evidence from multiringed structures on Ganymede and Callisto. *Icarus*, 44:454–471, November 1980. doi: 10.1016/0019-1035(80)90037-8.

H. J. Melosh. *Impact Cratering: A Geologic Process*. Oxford University Press, 1989a. ISBN 0-19-504284-0. Lunar and Planetary Laboratory, University of Arizona.

H. J. Melosh. Impact cratering: A geologic process, 1989b. p. 132.

H. J. Melosh. Impact cratering: A geologic process, 1989c. p. 177.

H. J. Melosh and W. B. McKinnon. The mechanics of ringed basin formation. *GRL*, 5: 985–988, November 1978. doi: 10.1029/GL005i011p00985.

J. J. Monaghan. Smoothed particle hydrodynamics. *ARA&A*, 30:543–574, 1992. doi: 10.1146/annurev.aa.30.090192.002551.

J. J. Monaghan and J. C. Lattanzio. A refined particle method for astrophysical problems. *A&A*, 149:135–143, August 1985.

D. Morrison and N. D. Morrison. Photometry of the gallilean satellites. In J. A. Burns, editor, *IAU Colloq. 28: Planetary Satellites*, pages 363–378, 1977.

K. Nagel, D. Breuer, and T. Spohn. A model for the interior structure, evolution, and differentiation of Callisto. *Icarus*, 169:402–412, June 2004. doi: 10.1016/j.icarus.2003.12.019.

NASA. A detailed view of callisto's surface, November 1996. URL http://solarsystem.nasa.gov/galileo/gallery/top10science-7.cfm. (last accessed: 26 Jan 2017).

Pioneer10/11 NASA. Sp-349/396 pioneer odyssey, January 1974. URL http://history.nasa.gov/SP-349/p180.htm. (last accessed: 8 Dec 2016).

W. H. Press, B. P. Flannery, S. A. Teukolsky, and W. T. Vetterling. *Numerical Recipes in Fortran 77*, volume 1. Cambridge University Press, 2 edition, February 1993. ISBN 9780521430647. p711, 713, 714.

C. Schäfer, S. Riecker, T. I. Maindl, R. Speith, S. Scherrer, and W. Kley. A smooth particle hydrodynamics code to model collisions between solid, self-gravitating objects. *A&A*, 590:A19, May 2016. doi: 10.1051/0004-6361/201528060.

C. M. Schäfer, S. Scherrer, R. Buchwald, T. I. Maindl, R. Speith, and W. Kley. Numerical simulations of regolith sampling processes. *P&SS*, 141:35–44, July 2017. doi: 10.1016/j.pss.2017.04.015.

P. M. Schenk. Ganymede and Callisto - Complex crater formation and planetary crusts. *JGR*, 96:15, August 1991. doi: 10.1029/91JE00932.

P. M. Schenk. Central pit and dome craters - Exposing the interiors of Ganymede and Callisto. *JGR*, 98:7475–7498, April 1993. doi: 10.1029/93JE00176.

P. M. Schenk. Thickness constraints on the icy shells of the galilean satellites from a comparison of crater shapes. *Nature*, 417:419–421, May 2002. doi: 10.1038/417419a.

P. M. Schenk and W. B. McKinnon. Ring geometry on Ganymede and Callisto. *Icarus*, 72:209–234, October 1987. doi: 10.1016/0019-1035(87)90126-6.

Asif A. Siddiqi. Deep space chronicle: A chronology of deep space and planetary probes 1958-2000. *Monographs in Aerospace History*, (24):94–97,102, June 2002. URL https://ntrs.nasa.gov/archive/nasa/casi.ntrs.nasa.gov/20020052429.pdf. (last accessed: 8 Dec 2016).

C. Thomas and R. C. Ghail. The Internal Structure of Callisto. In *Lunar and Planetary Science Conference*, volume 33 of *Lunar and Planetary Inst. Technical Report*, March 2002.

Astrogeology Science Center USGS. Callisto large ringed features, 2000. URL https://planetarynames.wr.usgs.gov/SearchResults?target=CALLISTO&featureType=Large%20ringed%20feature. (last accessed: 4 Jan 2017).

RPIF USGS Astrogeology Science Center. Callisto map, March 2016. URL https://astrogeology.usgs.gov/search/map/Callisto/Mosaic/callisto_map. (last accessed: 4 Jan 2017).

Dave Williams and Jay Friedlander. Voyager 1 callisto, March 1979. URL http://nssdc.gsfc.nasa.gov/imgcat/html/object_page/vg1_p21287.html. (last accessed: 21 Jan 2017).